



Integrated Arctic Observation System

Research and Innovation Action under EC Horizon2020
Grant Agreement no. 727890

Project coordinator:
Nansen Environmental and Remote Sensing Center, Norway


Deliverable 3.10

**Final implementation of the observing system:
Data delivery and report on results
of the observing systems in the coastal Greenland**

Start date of project:	01 December 2016	Duration:	60 months
Due date of deliverable:	30 May 2021	Actual submission date:	8 June
Lead beneficiary for preparing the deliverable:	GEUS		
Person-months used to produce deliverable:	25.5 pm		

Authors: Andreas P. Ahlstrøm, Antti Aarva, Teijo Arponen, Marcel Babin, Jason E. Box, Michele Citterio, Eva de Andrés, Robert S. Fausto, Johnna Holding, Jakob Jakobsen, Claudie Marec, Francisco Navarro, Roberta Pirazzini, Mikael Sejr, Evgeny Vasilenko

Version	DATE	CHANGE RECORDS	LEAD AUTHOR
1.0	01.03.2021	Template	A. Beszczynska-Möller
1.1	01.06.2021	Review version	A. P. Ahlstrøm
1.2	01.06.2021	Reviewed version	A. Beszczynska-Möller
1.3	04.06.2021	Final version reviewed by partners	P. Ahlstrøm
1.4	08.06.2021	Technical review and submission	K. Lygre

Approval	Date:	Sign.
X	4 June 2021	 Coordinator

USED PERSON-MONTHS FOR THIS DELIVERABLE					
No	Beneficiary	PM	No	Beneficiary	PM
1	NERSC		24	TDUE	
2	UiB		25	GINR	
3	IMR		48	UNEXE	
4	MISU		27	NIVA	
5	AWI		28	CNRS (Takuvik)	1
6	IOPAN		29	U Helsinki	
7	DTU		30	GFZ	
8	AU	2	31	ARMINE	
9	GEUS	12	32	IGPAN	
10	FMI	8	33	U SLASKI	
11	UNIS		34	BSC	
12	NORDECO		35	DNV GL	
13	SMHI		36	RIHMI-WDC	
14	USFD		37	NIERSC	
15	NUIM		38	WHOI	
16	IFREMER		39	SIO	
17	MPG		40	UAF	
18	EUROGOOS		41	U Laval	
19	EUROCEAN		42	ONC	
20	UPM	2.5	43	NMEFC	
21	UB		44	RADI	
22	UHAM		45	KOPRI	
23	NORCE		46	NIPR	
			47	PRIC	

Listed person-months (PM) include all work leading up to the deliverable.

DISSEMINATION LEVEL		
PU	Public, fully open	X
CO	Confidential, restricted under conditions set out in Model Grant Agreement	
CI	Classified, information as referred to in Commission Decision 2001/844/EC	

EXECUTIVE SUMMARY

This document, *Deliverable 3.10 - Final implementation of the observing system: Data delivery and report on results of the observing systems for the Coastal Greenland*, describes the final results and future perspectives, including data accessibility, of INTAROS WP3 Task 3.1 for the Coastal Greenland reference site, which is identified as a key location for freshwater output from the Greenland ice sheet to the ocean.

The work reported here from Task 3.1 describes a range of improvements on our monitoring capabilities for the entire journey of the freshwater flux from the Greenland ice sheet, through the fjords and into the ocean, including its impact on the marine ecosystem.

Below is a short summary of the results reported by each partner in INTAROS.

GEUS:

Data on snow water equivalent (SWE) successfully retrieved from SnowFox instruments and processed from four sites co-located with PROMICE weather stations, power supply issues were identified, and mitigation measures taken.

High-precision vertical and horizontal positional data was successfully retrieved from the new GNSS unit, capable of recording e.g., ice ablation by accurately recording changes in elevation. The deployment successfully tested a range of possible issues and a modified version of the device has already been implemented for landslide monitoring.

A rugged, precise and low-power tilt and azimuth sensor was developed and tested in the lab. Field test deployment is ongoing.

Corrected rain datasets from the ice sheet have been successfully retrieved and compared to results from regional climate models and reanalysis products.

All the demonstrated measurements above will be rolled out for additional PROMICE, GC-Net and GEM weather stations over the coming years and data made openly available through their respective databases.

AU:

Two years of CTD data so far successfully retrieved from the marine instruments deployed in Aug 2018 and again in 2019, with a third year expected by Aug 2021. It is planned to continue this monitoring as a part of the GEM monitoring programme.

Surface $p\text{CO}_2$ and carbonate parameters were observed during two coastal cruises in West Greenland 2016 and East Greenland 2018, respectively, to study the impact of freshening on CO_2 -uptake of the ocean, yielding 746 observations of the $p\text{CO}_2$ in the upper 50 m distributed among 120 stations.

(continued)

FMI:

Laboratory instrumentation and procedures to characterize the thermal and angular response of pyranometers, to increase the accuracy of the solar irradiance and albedo measurements were successfully applied to CNR1 and CNR4 net-radiometers of the PROMICE network. The method is expected to be applied to similar radiometers of the PROMICE, GC-Net and GEM monitoring networks in the future.

UPM:

Test flights delivered 200 km of good radar profiles over ice, proving the concept of the new helicopter-borne radar system in the field. The processed radar profiles have successfully yielded bedrock returns in usually difficult glaciological settings near glacier fronts, although partly disrupted by occurrence of meltwater and reflections off nearby nunataks.

CNRS-Takuvik:

More than 1900 profiles have been acquired so far with unprecedented sets of data with series measured under ice during wintertime. Takuvik intends to continue measuring sea-ice properties in Qikiqtarjuaq and other coastal ecosystems in Baffin Bay. The sensors developed at Takuvik will be integrated to a sea-ice endoscope in development at Université Laval, which will optimize the acquisition of data in situ over a wide range of sea-ice geometries.

Table of Contents

1. Introduction	7
2. Final implementation and operational use of the observing system for the Coastal Greenland	9
2.1. GEUS	9
2.1.1. Results of the final implementation of the observing system	9
2.1.2. Lessons learned and technology challenges identified during the project	19
2.1.3. Description of processing and analysis of the obtained data	25
2.1.4. Accessibility of the obtained data sets and repositories used	35
2.1.5. Future plans for operation of the observing system, including data provision	36
2.2. AU	39
2.2.1. Results of the final implementation of the observing system	39
2.2.2. Lessons learned and technology challenges identified during the project	40
2.2.3. Description of processing and analysis of the obtained data	40
2.2.4. Accessibility of the obtained data sets and repositories used	41
2.2.5. Future plans for operation of the observing system, including data provision	41
2.3. FMI	42
2.3.1. Results of the final implementation of the laboratory facilities to characterize optical sensors - upgrade of the PROMICE pyranometers through laboratory characterization	42
2.3.2. Lessons learned and technology challenges identified during the project	45
2.3.3. Description of processing and derivation of the correction equations	45
2.3.4. Accessibility of the obtained upgraded data sets and repositories used	52
2.3.5. Future plans for operation of the observing system, including data provision	52
2.4. UPM	53
2.4.1. Results of the final implementation of the observing system	53
2.4.2. Lessons learned and technology challenges identified during the project	54
2.4.3. Description of processing and analysis of the obtained data	55
2.4.4. Accessibility of the obtained data sets and repositories used	56
2.4.5. Future plans for operation of the observing system, including data provision	56
2.5. CNRS-Takuvik	57
2.5.1. Results of the final implementation of the observing system	57

2.5.2.	Lessons learned and technology challenges identified during the project	57
2.5.3.	Description of processing and analysis of the obtained data	58
2.5.4.	Accessibility of the obtained data sets and repositories used	58
2.5.5.	Future plans for operation of the observing system, including data provision	58
3.	Performance and fitness-to-purpose of the platforms, sensors and systems implemented during INTAROS for a future sustained Arctic observing system	60
3.1.	GEUS	60
3.2.	AU	62
3.3.	FMI	62
3.4.	UPM	63
3.5.	CNRS-Takuvik	63
4.	Summary	64
5.	Literature	68

1. Introduction

INTAROS aims to develop and implement innovative solutions and new technologies to fill selected gaps identified in the existing observing systems in the INTAROS gap assessment (WP2) and prior efforts. The plan is to accomplish this aim by integration of novel instruments and sampling methods with mature components of existing observatories to increase temporal and geographic coverage of in situ observational data in the Arctic and include key parameters which are currently missing.

Three reference sites were selected within INTAROS as providing critical data to understand ongoing climate and environmental changes and their consequences for the Arctic. This report is focused on describing the final implementation of the observing system in WP3 for one of these, namely Coastal Greenland, which is identified as a key location for freshwater output from the Greenland ice sheet to the ocean.

As the intention in WP3 has been to optimize the fieldwork effort and maintain the integrity of new data, we have built on and effectively extended infrastructure already existing in selected reference sites and distributed observatories. Over the duration of the WP3 deployment phase, new sensors, integrated platforms and experimental setups have been implemented with the intention of sustained use in a future iAOS. New collected data has been pre-processed under WP3 to provide standardized data sets ready for integration in WP5, demonstration actions in WP6, and for the consultations with stakeholders in WP7.

The activities in the coastal region of Greenland covered in Task 3.1 on which this report is focused, include a range of actions both offshore, onshore and on the Greenland ice sheet to monitor identified environmental variables. Specifically, these include:

- A combination of ocean moorings with new solutions for the Northeast Greenland site to obtain coverage, duration, thickness and energy balance of snow cover on sea ice to increase knowledge of how freshening of the Arctic impacts the marine ecosystem.
- Establishment of an essential baseline dataset on surface $p\text{CO}_2$ and carbonate parameters for the entire Greenland coastal zone, enabling future monitoring of the impact of freshening on CO_2 uptake and acidification of the ocean.
- Implementation of a novel ruggedized system adding to the existing on-ice PROMICE weather station network for measuring snow-water equivalent on the ice sheet margin, in order to capture meltwater retention mechanisms in the snow and firn on the ice - a main uncertainty in modelling of future ice sheet runoff and key to the meltwater output to the ocean from the Greenland ice sheet.

- Addition of precise positioning capability of the same on-ice sheet network will provide much needed calibration for satellite-derived ice velocity maps used to calculate the ice-dynamic mass loss to the ocean and monitor potential feedbacks between meltwater formation and ice dynamics.
- The addition of rain gauges to the in-situ PROMICE automatic weather stations on the Greenland ice sheet in order to capture the transition of a precipitation regime dominated by snow to one with frequent rain events.
- Improvement of the accuracy and spatial representativeness of the in-situ snow albedo observations (from PROMICE and GC-Net networks) over Greenland ice sheet through improved instrument characterization as well as a methodology for correction of in-situ ice sheet albedo measurements.
- Improvement of an innovative ice-penetrating radar system for generating ice thickness data over highly crevassed ice-sheet outlet glaciers.
- Implementation of a multi-disciplinary approach to study the ice-driven dynamics of the Arctic coastal ecosystems in the Young Sound (with similar system in Kongsfjorden under Task 3.3 for a comparison of two contrasted fjords), by merging physical oceanography and marine biology, and using the passive acoustics non-invasive technique to characterize both physical (dynamics of sea ice and icebergs, waves-ice interactions) and biological compartments (behavior of organisms at different trophic levels).
- Contribution to a suite of sensors for automated monitoring of the spring bloom processes and the bio-optical and biogeochemical properties under the ice pack of the coastal ocean at the Baffin Bay Observatory (in Qiqiktarjuak).

A number of these activities have been affected by the COVID-19 pandemic which severely limited and still limits the access to the field sites in and around Greenland, as is the case for much of the Arctic region. This implies that some activities have lost entire field seasons, which is a huge setback considering the prudent requirement to test instruments and methodologies thoroughly in the field, before allowing a full-scale deployment as a new part of an established monitoring or observing system. Yet, as this report testifies, the majority of the significant advances and innovations expected for the coastal Greenland observing system in INTAROS have been accomplished despite difficult circumstances.

2. Final implementation and operational use of the observing system for the Coastal Greenland

2.1. GEUS

Contributors: Andreas P. Ahlstrøm, Robert S. Fausto, Michele Citterio, Jason E. Box, Jakob Jakobsen

2.1.1. Results of the final implementation of the observing system

Results from measuring snow water equivalent on the Greenland ice sheet

Accurate measurements and long term in-situ monitoring of climate and surface mass balance of the Greenland ice sheet is crucial to assess the surface and near-surface atmospheric conditions in a changing climate. In situ measurements are also important for process understanding and model development to achieve accurate forecasts of the total mass budget for better estimates of future changes in the global sea-level from Greenland ice sheet. An important factor in the total mass budget of the ice sheet is the mass gain from snowfall during the winter season, which is a major positive term in total budget.

The Geological survey of Denmark and Greenland (GEUS) established the Programme for monitoring of the Greenland ice sheet (PROMICE) in 2007, which in part maintains a network of automatic weather stations (AWSs) mostly located on ice in the ablation area of the ice sheet. The network measures atmospheric variables, incoming and outgoing radiation, ice temperature, and height changes due to snow and ice ablation. Quantifying the snow mass from height changes due to snowfall is a challenge because of changes in snow density of the snowpack throughout the season. In this report, we present a new instrument, which measure the snow water equivalent (SWE) or snow mass of the snowpack on top of the sensor, from 5 locations in the ablation area of the Greenland ice sheet. We describe the data set production chain and methods followed by a presentation of the data.

The new instrument, SnowFox, measures SWE through the attenuation of cosmic ray generated neutrons. The sensor records neutron events over a regular time-interval. To derive SWE, the raw neutron counting rate of the sensor must be corrected for variations in barometric pressure and solar activity. The corrected neutron counting rate is then normalized to a no-snow reference counting rate. Any subsequent counting rate will decrease exponentially as a function of the amount of SWE overlying the detector.

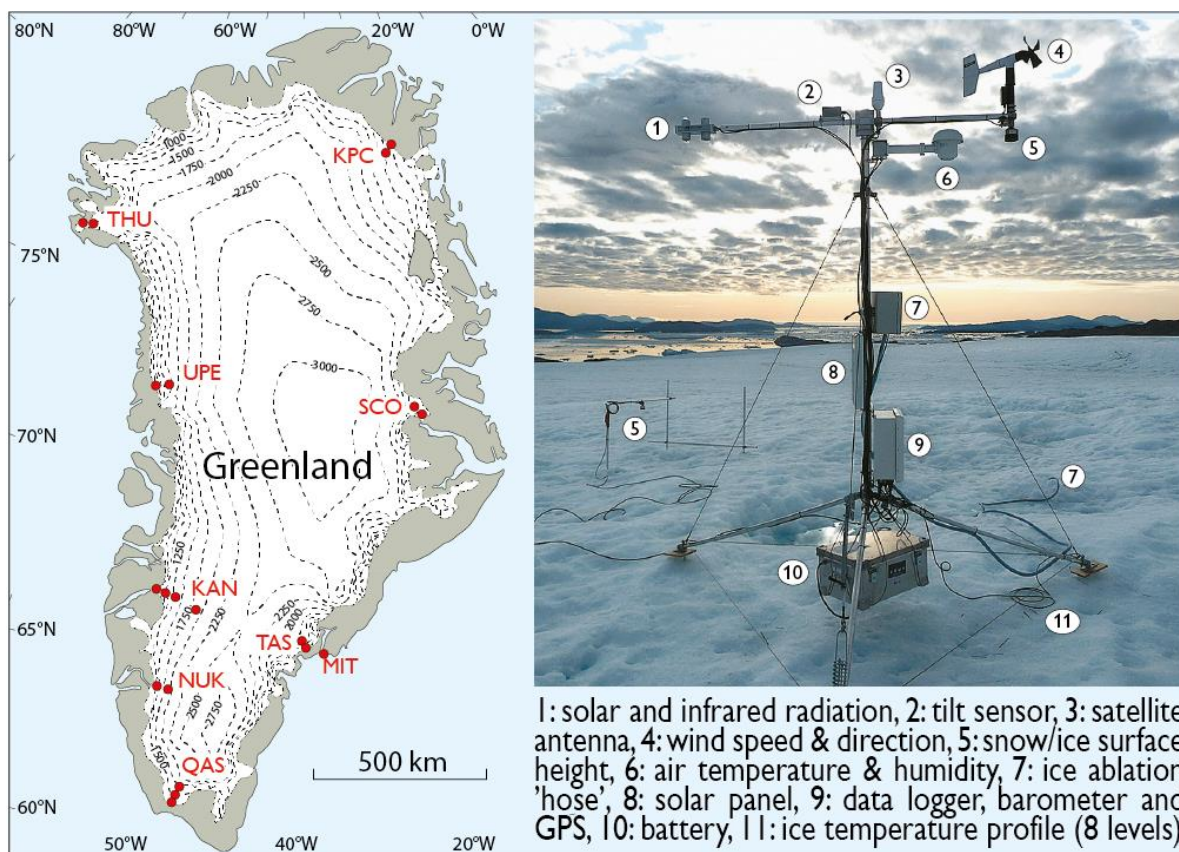


Figure 1: PROMICE locations with AWSs at different elevations (left). PROMICE AWS UPE_L photographed on 17 August 2009.

In 2018, we installed five SnowFox instruments at four PROMICE locations, namely Tasiilaq (TAS), Qassimiut (QAS), Kangerlussuaq (KAN), and Thule (THU) (Figure 1) during snow free condition, except for the THU region, which was placed in a snow pit. Two sensors were deployed at the QAS transect at different elevation to measure the altitudinal gradient in SWE. Initial testing of the system and sensor found an optimal configuration for deployment onto the ice sheet. The optimal configuration was a 4-hour counting period every day to conserve power, except for QAS_M, where we experimented with measurement interval of 2 days. We mounted the SnowFox loggerbox on a “stand alone” PROMICE tripod together with a solar panel and a battery box with six Panasonic (28 Ah, in total 156 Ah) batteries inside (Figure 2a).

In 2020, we added a windmill to the QAS_M setup to recharge the batteries when the solar panel is not able to provide power. We still await the results from this setup. The SWE sensor (SnowFox) was placed next to the tripod on ice so that it could be buried by snow during the accumulations season.

During the 2019 field season, we retrieved the data from all deployed SnowFoxes, but we had some problems with power in four places because of either too much snow that buried our solar panel or too little sunlight in the winter months to recharge the batteries (Figure 2b).

For the THU location, we installed the SnowFox at the bottom of a snowpit in an excavated hole under the snow to get a measurement of an undisturbed snowpack. We manually measured the bulk density of the snowpack to be $380 \pm 13 \text{ kg m}^{-3}$, while the SnowFox measurement showed a $33.5 \pm 1.6 \text{ cm}$ water equivalent or ca. $372 \pm 18 \text{ kg m}^{-3}$ based on a 90 cm thick snowpack on top of the sensor. The uncertainty of the SnowFox measurement is based on the standard deviation of a 17- day long period with subfreezing condition and no detected snowfall. The standard deviation is twice as high as the one obtained from Howat et al. (2018) based on their installation near Summit.

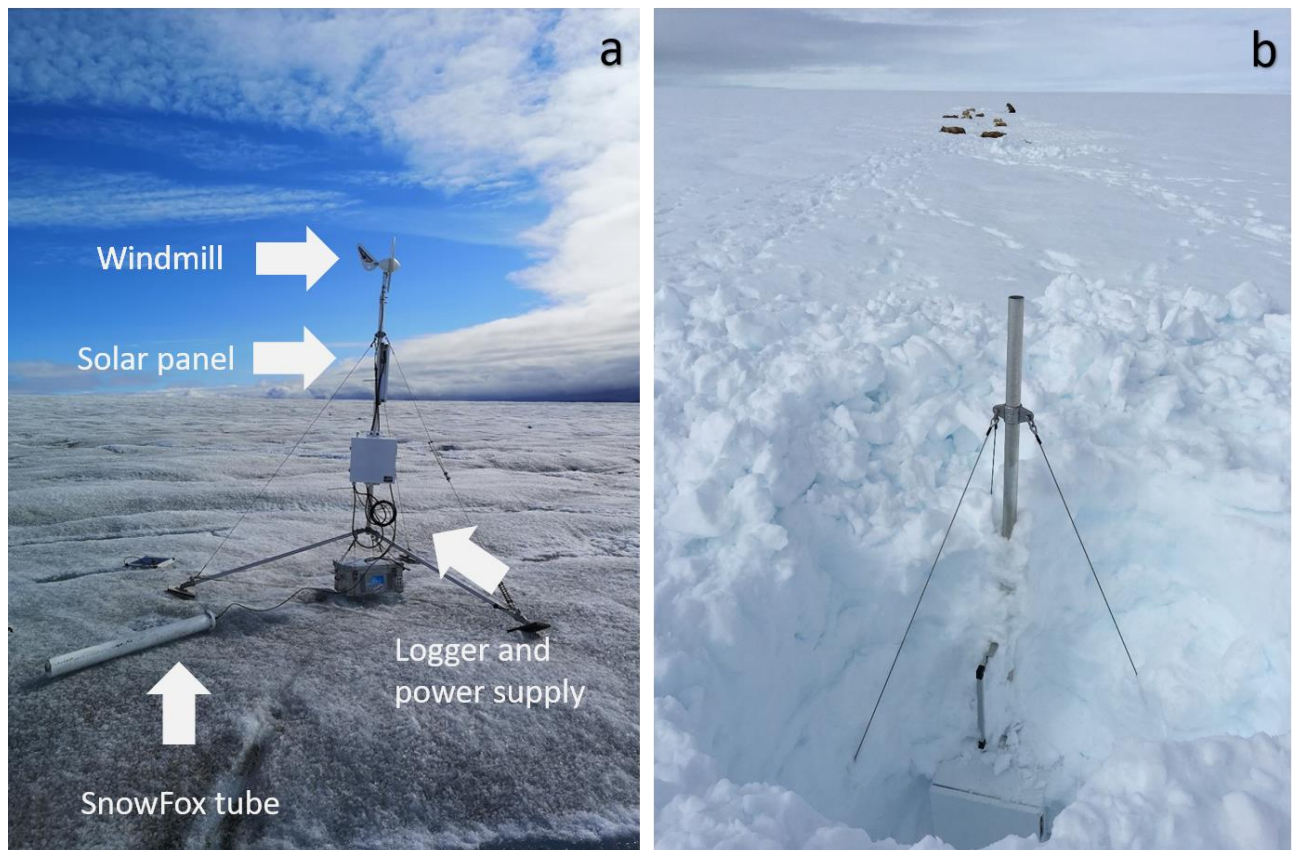


Figure 2: SnowFox: a) end melt season 2020 at QAS_M site b) end accumulation season at the TAS_A site spring 2019.

Results from high accuracy GNSS positioning

The main focus of this system is on minimizing power consumption so that battery powered operation is possible through the polar night while still providing high accuracy positions. This was achieved by selecting the Septentrio AsteRx-m receiver, one of the lowest power GNSS receiver modules available on the market that receives both L1 and L2 bands. Dual frequency receivers use significantly more power than single frequency receivers, and are much more expensive, but ionosphere effects, the largest term in the uncertainty of GNSS observables, can be corrected autonomously by the receiver when signals are received at different frequencies.

During the course of the project, the manufacturer Septentrio introduced a newer model AsteRx-m2 which is capable of receiving Galileo signals in addition to GPS and GLONASS, and a third frequency (L5) with only a modest increase in power.

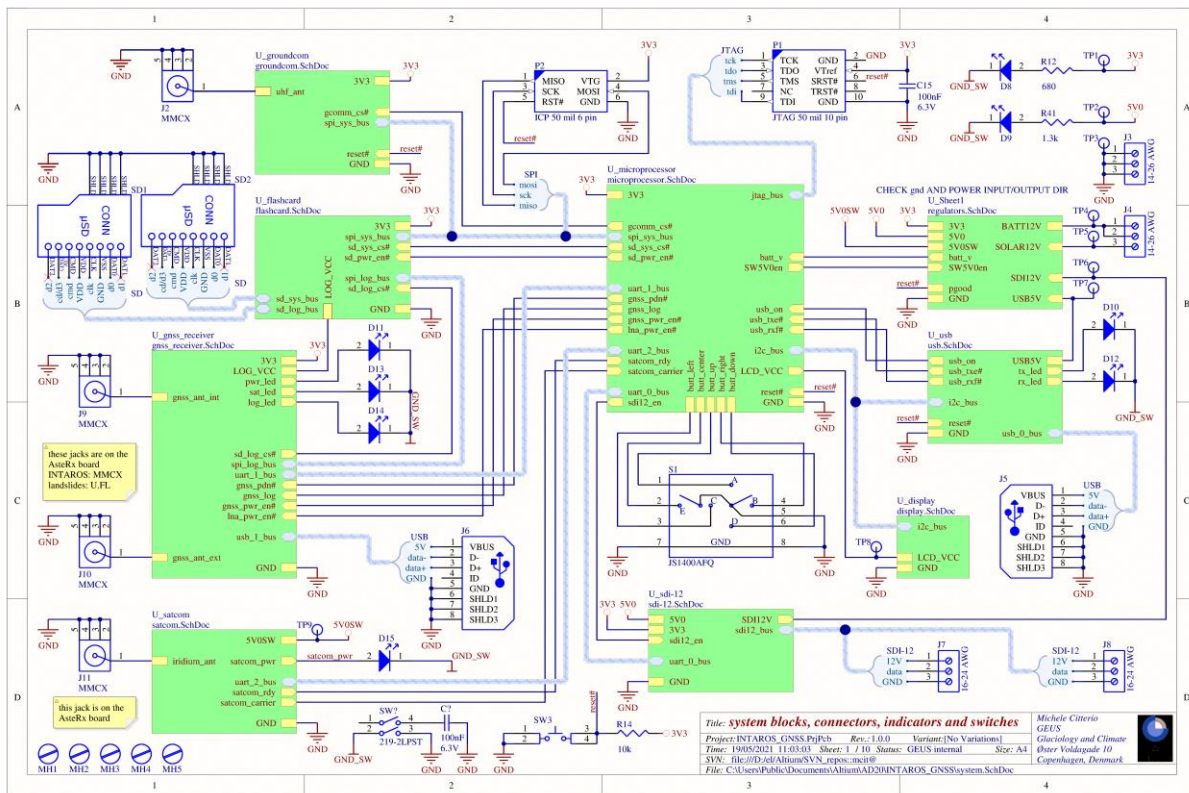


Figure 3: System-level schematic of the INTAROS high accuracy GNSS receiver, showing the individual submodules as green blocks (microcontroller, AsteRx-m/m-2 submodule, power regulators, USB interface, SDI-12 interface, Iridium SBD satcom, optional ground UHF radio, flashcards interface, LCD display). The diagram also shows all connectors, switches and indicator LEDs.

Our current system is compatible with both AsteRx-m and -m2 models. It includes the ability to transmit a position via Iridium SBD (short burst of data) and to connect to a standard GEUS AWS (automatic weather station) using the SDI-12 serial interface (Figure 3), and to locally log to a flashcard the raw GNSS observables needed for postprocessing.

The amount of these data is too large for transmission over the Iridium SBD link both from an airtime costs and from a power consumption perspective. For ease of testing in the field, and for applications where the SDI-12 interface is not available, a USB interface is provided which is also capable of powering up the entire system (with the exception of the Iridium SBD satellite modem).

The second USB connector is only needed for upgrading the AsteRx firmware in the field without removing the module. A JTAG (Joint Test Action Group) port simplifies debugging of the firmware and it can also be used as an alternative to the ICP (in-circuit programming) port for programming and updating of the microcontroller firmware. The hardware includes experimental support for an optional LoRa (Long Range) radio for connecting to other GNSS receivers within a radius of some km and operate in differential mode.

Power can be supplied from 12 V solar panels, a 12 V VRLA (valve regulated lead acid) battery, the USB interface and the SDI-12 interface. All power sources can be connected without interfering with each other. The solar panels can charge the battery however care is needed in dimensioning these two components as no charge regulation is provided.

This is similar to the power supply used by the GEUS AWS and relies on the ability of VRLA batteries to withstand overcharge at very low rates without damage. From experience, the ratio between the nominal power output of the solar panel and the total battery capacity should be smaller than 0.01 W/Wh.

To further minimize power consumption, the system is suitable for use with a passive GNSS antenna. This mandates the use of very short and low loss coaxial cables between antenna and receiver, and to accept lower signal levels. The observed signal levels from the 2019-2020 field deployment will be shown in Section 2.1.2 for a passive Novatel Pinwheel GPS-704-X antenna.

If desired, it is also possible to use active antennas, with power supplied by the receiver through the antenna cable. In this case the antenna supply voltage is limited to maximum 5V, which is adequate for most recent antennas including the active versions of Novatel Pinwheel such as type GPS-703-GGG.

Inside the instrument, power consumption is minimized by turning off unnecessary hardware using the programmable low power modes of the chips, when available, or by removing power from parts of the circuit. The only permanently running function is timekeeping, which has a coin cell battery backup in case no external power source is available, as during shipping.

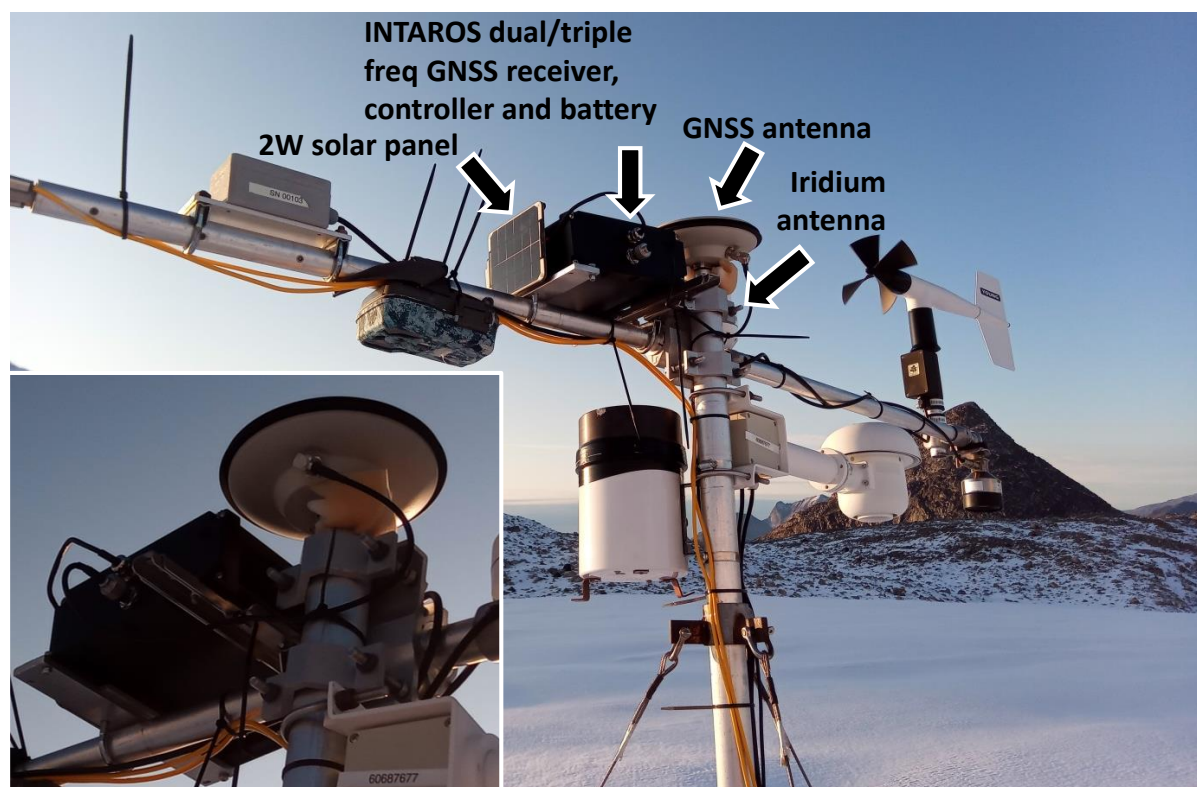


Figure 4: Self contained system as deployed on Qasigianguit Glacier close to Nuuk, Greenland, upon installation at the end of August 2019.

The installed system in Figure 4 shows the test field deployment at the PROMICE AWS on Qasigianguit Glacier close to Nuuk between August 2019 and August 2020, which was independent both in power supply and data logging from the AWS. This was essential in order to avoid impacting the normal meteorological and glaciological monitoring in case of unexpected behavior or malfunction of the GNSS device.

To keep weight acceptable, the configuration of the Qasigianguit Glacier test unit had a smaller battery than needed for uninterrupted operation during winter. However, this let us verify the proper behavior upon recovering from low battery conditions.

Results from the new radiometer tilt and azimuth instrument

The instrument measures the tilt and azimuth of the Kipp & Zonen CNR-1 and CNR-4 radiometers carried by the PROMICE AWS and outputs analog voltages as well as digital values in decimal degrees with a resolution of 0.1 degree. This is needed for correcting the radiation measurements because AWS operating on ice cannot provide a stable level orientation of the radiometers.

The INTAROS instrument is composed of a control board carrying a precision 2-axes accelerometer and tilt meter type ADIS16209 by Analog Devices (USA) and a solid-state electronic compass type HMC6343 by Honeywell (USA).

The HMC3443 is also capable of measuring tilt, however not at the sub-degree accuracy required by our application. The tilt information from the HMC6343 is therefore only used internally as a confidence check for the ADIS16209 measurements and as a fallback in case the ADIS16209 fails.

As will be discussed in detail in a following section, data loss impacted the 2019-2020 field deployment. In this section we summarize the results of the pre-deployment tests showing the performance of the sensors compared to the legacy tilt-only sensor on the PROMICE AWS.

The development of this sensor was delayed initially due to ca. 9 months lead time for the ADIS16209 tilt sensor and then in the first half of 2019 due to problems with powering and interfacing to the ADIS16209, resulting in occasional lock-ups during testing, as well as difficulties implementing the planned serial communication using the SDI-12 protocol.

To sidestep the difficulties with implementing the SDI-12 protocol and to speed up the adoption of the new INTAROS instrument at as many GEUS AWS as possible, an analog output interface has been added that mimics the output signals of the 2-axes tilt meter currently in use.

Between 25 degrees from the horizon on each axis, the analog output is proportional to the tilt and ranges between -2.5 and +2.5 V with a linear coefficient of $10^\circ/\text{V}$. This matches the full range covered by the previous sensor used on the GEUS AWS, and without requiring the linearization correction needed by the older sensor.

The INTAROS instrument can further measure all the way to +/- 90 degrees and while correcting radiation measurements becomes increasingly difficult at steeper angles, high tilt is an important diagnostic information for the planning of the field maintenance visits. For this reason, the INTAROS device also outputs angles between 25 and 90 degrees with no loss of resolution through the serial interface and with a higher linear coefficient of $30^\circ/\text{V}$ on the analog interface.

A performance comparison in the lab between 3 different INTAROS prototype units and the tilt sensor currently used on the GEUS AWS is shown in Figure 5, where the residual error of the old sensor is plotted after correction for the non-linear response while the INTAROS instrument does not require such correction.

The INTAROS hardware supports an improved correction for non-zero offset at level angle and for measurement of drift due to temperature fluctuations, but these have not yet been implemented in the firmware.

Low power consumption was a key design goal and it corresponds to a peak of 250 mW while performing the tilt and azimuth measurement, followed by a stable 30 mW power consumption while the measurement is being transferred to the datalogger.

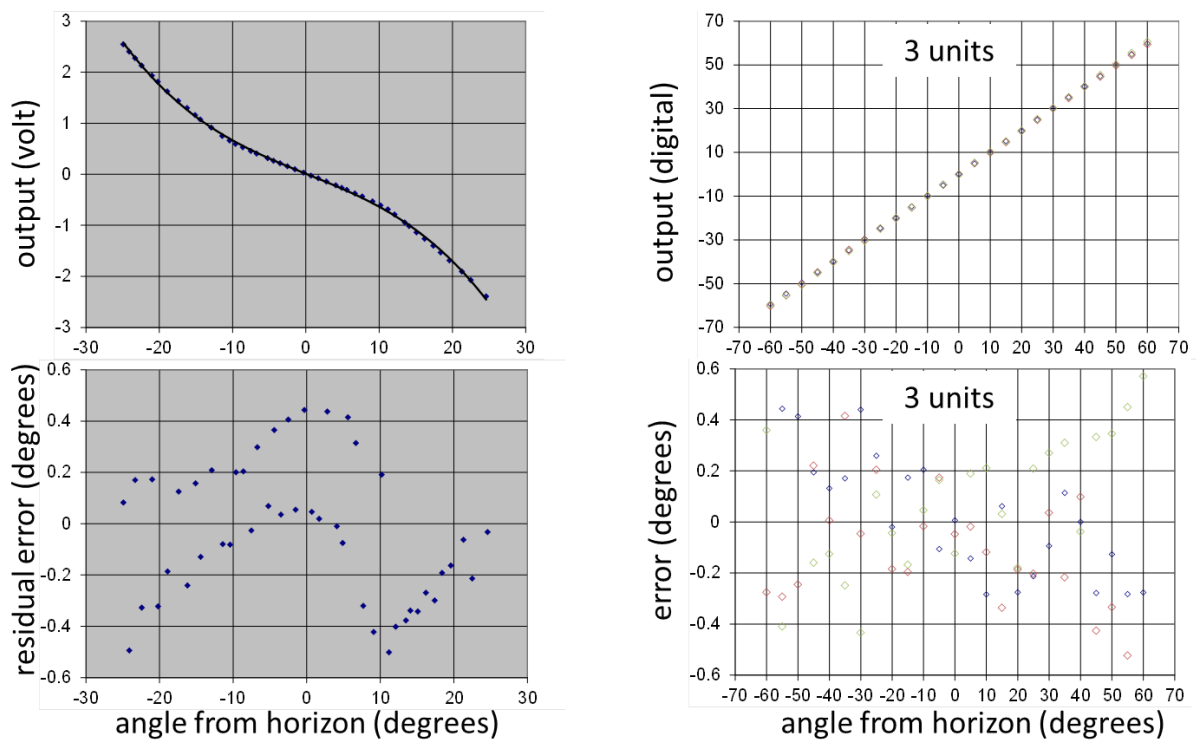


Figure 5: comparison of tilt and tilt error measured with the current sensor used on the GEUS AWS (left) and the new INTAROS sensor (right).

Results of the final implementation of rain gauges on ice sheet AWS

Since 2016, the Geological Survey of Denmark and Greenland has maintained precipitation measurements in Greenland, emphasizing on-ice locations, namely: the Qagssimiut ice lobe of the southern ice sheet (QAS) and the K-transect east of Kangerlussuaq (KAN) (Figure 6) (Table 1: Greenland locations with INTAROS liquid precipitation gauge data).

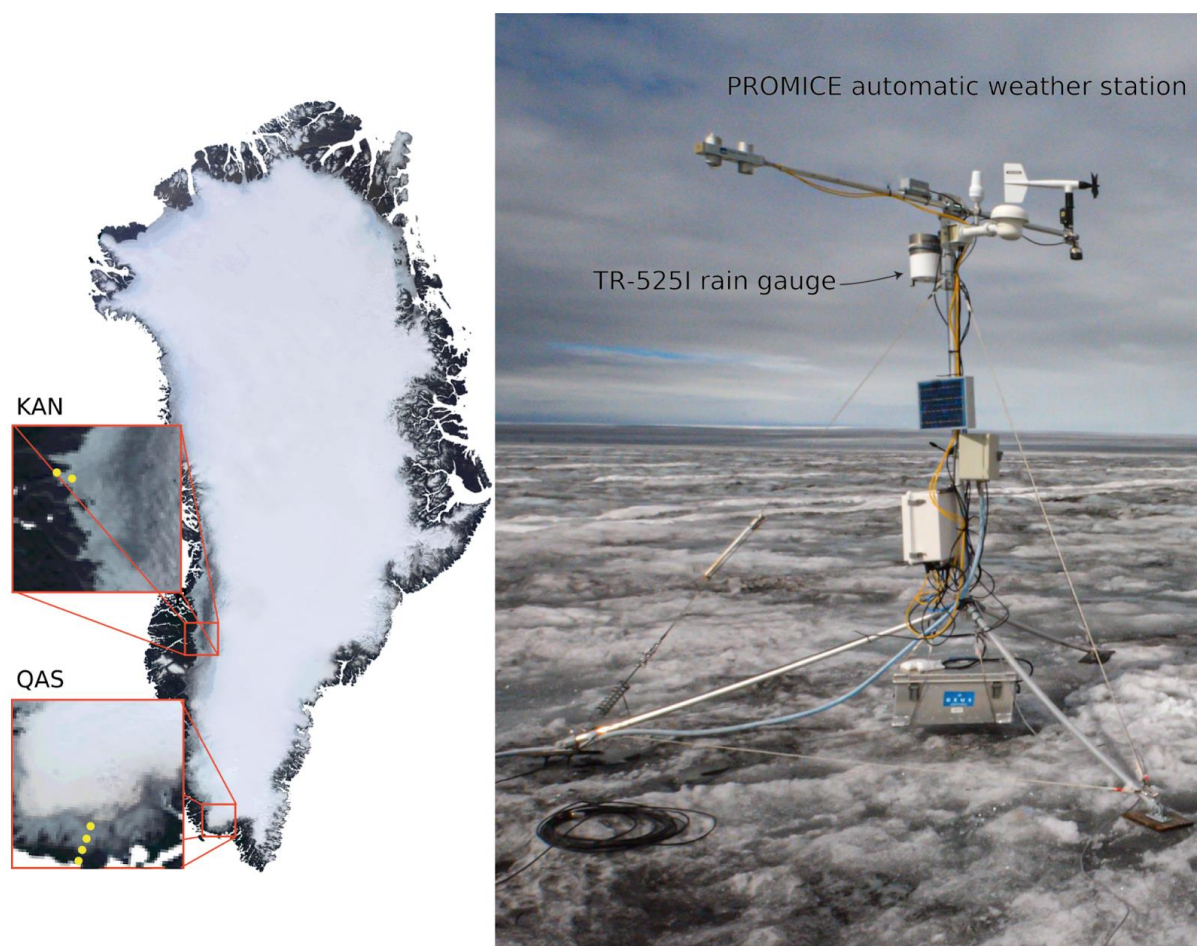


Figure 6: (left), Greenland ice sheet rain gauge locations and (right) example illustration of rain gauge placement near the top of the QAS_U PROMICE AWS mast Aug. 29, 2020.

Table 1: Greenland locations with INTAROS liquid precipitation gauge data.

site	latitude deg. N	longitude deg.	Elevation m	date of first recording	date of last available recording	timespan of measurements years	number of days with rain recorded	land surface type
QAS L-16	60.951	-46.938	20	6/9/2018	7/4/2020	2.1	208	land
QAS_L	61.031	-46.849	271	8/10/2016	8/21/2020	3.9	282	ice sheet
QAS_M	61.099	-46.833	621	8/10/2016	8/21/2020	3.9	301	ice sheet
QAS_U	61.174	-46.820	893	8/30/2018	8/21/2020	2.3	148	ice sheet
KAN_L	67.095	-49.953	664	8/31/2017	11/19/2018	1.2	62	ice sheet
KAN_B	67.125	-50.183	350	4/18/2016	9/20/2016	0.4	33	land

Objectives

Results from the new GEUS rainfall data are currently in the form of a comparison of the field data with two state-of-the-art regional climate models. The EU Copernicus Climate Change

Service (C3S) and its Arctic Regional ReAnalysis (CARRA) dataset is of particular interest because it assimilates a wide range of in-situ meteorological data from Greenland. The other model data is the well-known ERA5 dataset.

CARRA

The CARRA reanalysis system (Yang et al., 2020), applies HARMONIE-AROME, a non-hydrostatic, convection-resolving weather forecast model (Bengtsson et al., 2017) to assimilate an extensive collection of observations within the Greenland domain at 2.5 km horizontal grid spacing. CARRA rainfall intensity is estimated from an approach that lies in the middle of seven phase identification approaches evaluated by Huei et al. (2021) with total precipitation with the transition air temperature from snow to rain set to vary linearly 1°C above and below 1.5°C after (Hock and Holmgren, 2005; Rohrer, 1989).

ERA5

ERA5 is the fifth generation of global reanalysis from ECMWF (Hersbach et al., 2020; Copernicus Climate Change Service Climate Data Store (CDS), n.d.) and is based on the Integrated Forecasting System (IFS) Cy41r2, operational at ECMWF in 2016. ERA5 therefore benefits from a decade of developments in model physics, core dynamics and data assimilation compared to its predecessors. In addition, ERA5 includes a substantial improvement in spatial (31 km horizontal grid spacing) and temporal (hourly output) resolution compared to the previous product (ERA-Interim), which was discontinued on 31 August 2019. By assimilating historical observations into a state-of-the-art numerical weather prediction model, ERA5 provides spatial and temporal consistent estimates of atmospheric and surface variables, including an uncertainty estimate based on a ten-member ensemble run at lower resolution. ERA5 improves in general upon ERA-Interim, e.g., for global precipitation estimates (Hersbach et al., 2020).

Results of the comparison of observations to simulations

CARRA rainfall simulations agree consistently more with the field data than the ERA5 data, both in the ratio of totals and the correlations. Higher agreement for CARRA is likely due to the higher horizontal resolution in CARRA and that modelled atmosphere from CARRA is initialized at PROMICE and other locations within the model domain. Also, CARRA data includes explicitly modelled hydrometeor interactions in the convection-permitting model physics of HARMONIE-AROME.

Table 2: Comparison of rainfall estimates from field data versus two regional climate models.

model	site	correlation	weighted average correlation	Σ observations ÷ Σ model	Σ observations ÷ Σ model	days with observed and modeled rain	Σ rain observations mm	average tilt	average correction factor
ERA5	L-16	0.6	0.60	1.8	1.6	52	1069	3.5	1.14
	QAS_L	0.8		1.6		87	1754	4	1.11
	QAS_M	0.9		1.6		47	1064	4.1	1.14
	QAS_U	0.7		1.0		23	298	16	1.13
	KAN_L	nan				2			
	KAN_B	-0.1		1.2		3	11		1.11
CARRA	QAS_L-16	0.421	0.80	1.19	0.9	33	362	3	1.13

	QAS_L	0.873		0.98	69	1537	3.8	1.12
	QAS_M	0.943		0.79	56	1013	4.3	1.13
	QAS_U	0.734		0.79	21	258	18.7	1.12
	KAN_L	0.475		0.79	10	50	9.6	1.12
	KAN_B	0.569		0.93	5	23		1.05

2.1.2. Lessons learned and technology challenges identified during the project

Lessons learned on measuring SWE on the Greenland ice sheet

The new SWE sensor complement the existing PROMICE monitoring efforts by measuring the mass of an overlying snowpack. Including the SWE sensor in the PROMICE AWS system complete the monitoring of all the major components in the surface balance budget. In general, the sensor works, but the system needs a lot of power to measure and record the neutron counts. The SWE measurements will still be kept as separately systems alongside the PROMICE station in order not to jeopardize the core station operation. Eventually, the SnowFox will be integrated in the standard station setup and established at all the stations when we have tested the combined windmill-solar panel setup at QAS_M successfully.

Lessons learned regarding high accuracy GNSS positioning

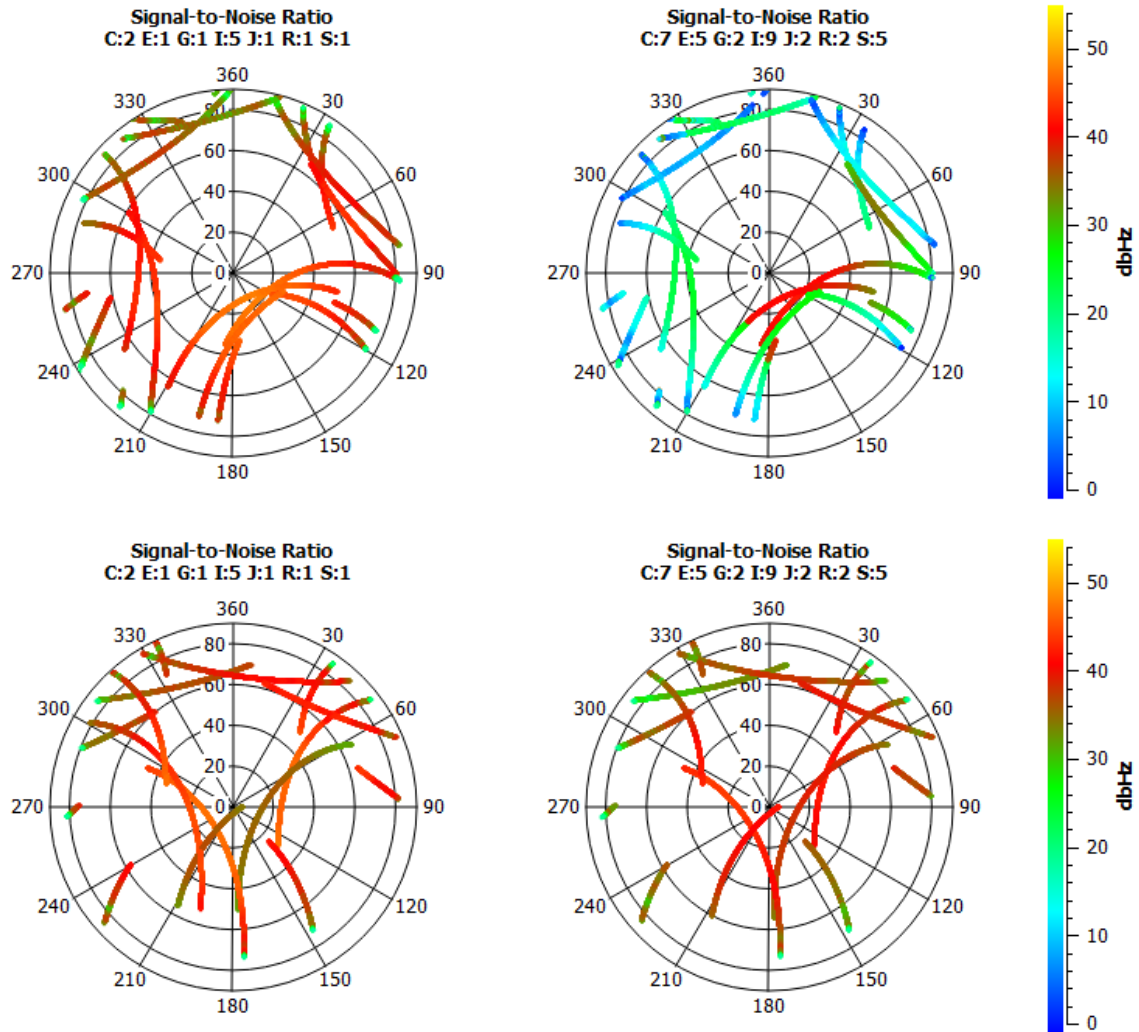
The most valuable information obtained by the end of the 2019-2020 field deployment concerns the performance achievable under realistic conditions with a compact and low power GNSS receiver that can be installed on the tripod of a standard GEUS AWS and in close proximity with potentially interfering systems such as the Iridium SBD modem.

The same type of AWS is used by PROMICE at 20 stations on the Greenland Ice Sheet (GrIS), by GlacioBasis at 6 stations on glaciers and ice caps independent from the GrIS, and it can fit as cabin payload on a Eurocopter AS350, the most cost-effective helicopter commonly available in Greenland.

The performance of the Novatel GPS-704-X passive antenna combined with the comparatively high gain of the input amplifier of the Septentrio AsteRx receivers proved to be adequate when connected through a short (0.5 m) and low loss antenna cable. Passive antennas may become even more important with the release, after INTAROS had already started, of even lower power and lower cost dual frequency receivers.

Figure 7 shows an example (DOY 96, year 2020) of the SNR (signal-to-noise ratio) for the L1 and L2 frequency bands for both GPS and GLONASS. Signal strength is satisfactory except for the comparatively weak GPS L2 signals (top right plot). However, the reason for the sudden change in SNR for 3 of these otherwise weaker signals is unclear and it may suggest a suboptimal configuration of the hardware that may be improved in the future.

To provide a complete picture of the antenna performance, the elevation mask was set to 0° above the horizon both in the GNSS receiver and the postprocessing software. This station is located on the lower part of a north-facing glacier so the surrounding topography limits somewhat the visibility of satellites, particularly toward south.



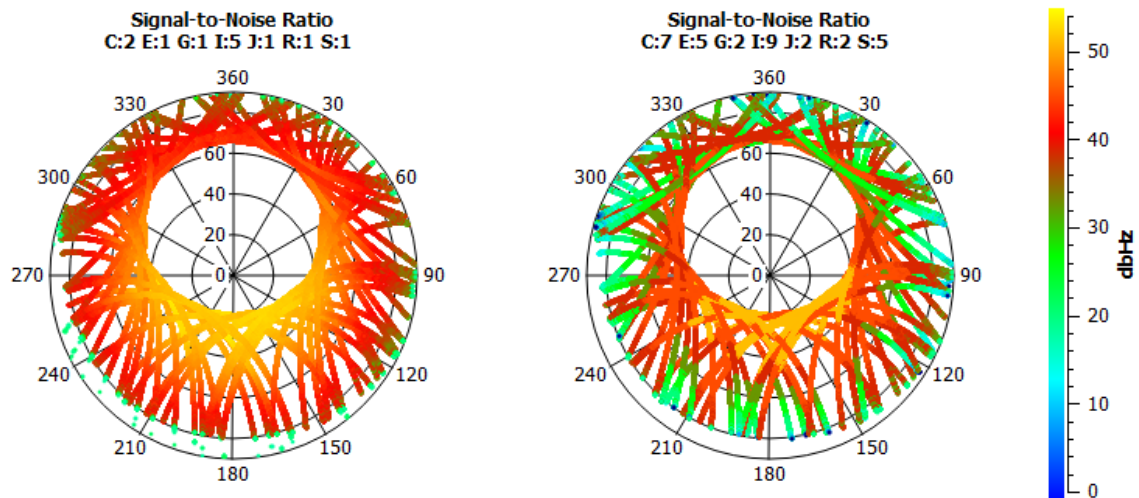


Figure 7: Plots of SNR over the same 3.5 hours interval for GPS (top) and GLONASS (middle) signals in the L1 (left) and L2 (right) frequency bands. Higher values represent stronger signals. For comparison, GPS SNR over a full day from the permanent G-Net QAAR station in Qaarsut (bottom row). Higher values represent stronger signals.

While somewhat lower than commonly observed using active antennas, as in the example shown for the permanent G-Net station in Qaarsut, the overall SNR performance of our passive antenna appears adequate. Figure 8 shows the ability of the receiver to maintain almost uninterrupted tracking of GPS, GLONASS and Galileo signals. As generally expected, gaps and cycle slips mostly occur at the beginning and end of each satellite traverse, when the satellite is very low above the horizon.

While arguably an uncommon configuration often recommended against by manufacturers, the good performance of a passive antenna is not surprising when considering that signal loss over a short coaxial cable and some connectors can be kept below the noise figure of a typical low noise amplifier (LNA).

Combining all three constellations, the number of satellites in view and tracked rapidly reaches 25-30 after a few minutes from the receiver is powered on. This is a very good result especially considering that the mountains surrounding Qasigianguit Glacier obstruct parts of the sky, contrary to the completely open sky typical of ice sheet sites.

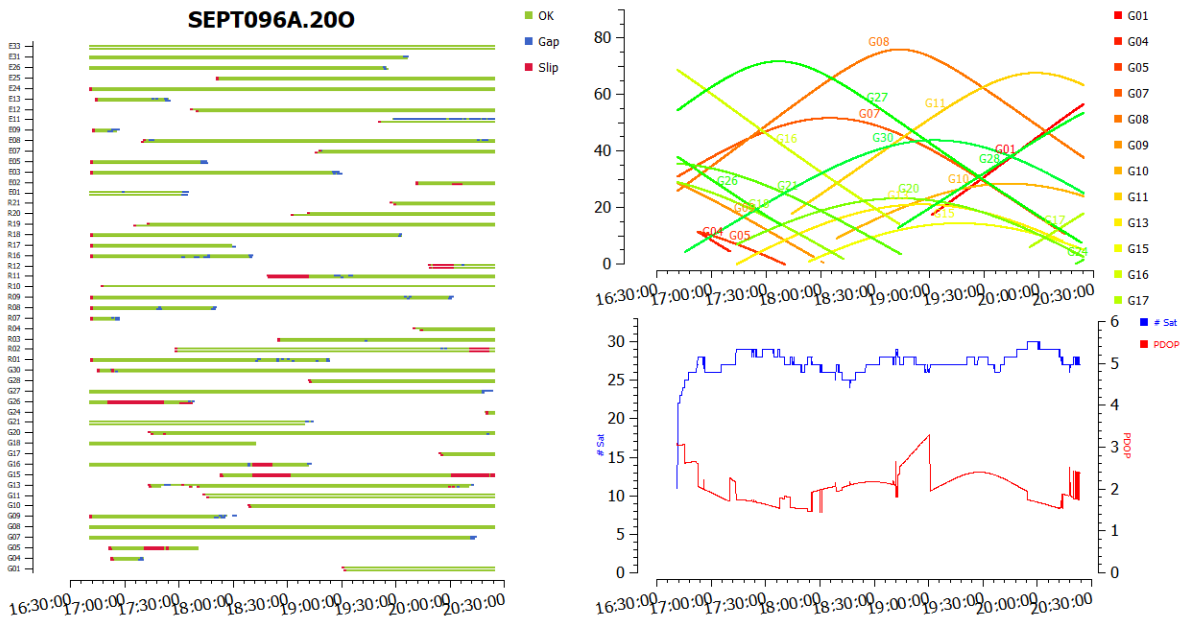


Figure 8: Tracking information for GPS (G), GLONASS (R) and Galileo (E) signals (left); corresponding plots of GPS satellites elevation (top right) and total number of tracked satellites with resulting position dilution of precision (PDOP, bottom right).

From a system integration point of view, it is remarkable that no cycle slips or loss of tracking seem to occur at full hours, when the AWS transmits the hourly weather report through the Iridium SBD satellite service. The frequency band allocated to Iridium is adjacent to the upper limit of the GNSS L1 band, and the transmitting antenna produces a signal ca. 15 orders of magnitude more powerful than the GNSS signals at ground level. Because of the risk for interference and even physical damage from overload of the receiver input, several experiments had been carried during development in Denmark to identify a safe distance from a transmitting Iridium antenna.

After very little interference and no noticeable overload damage could be observed, the GNSS antenna in the test deployment was deliberately installed in very close proximity (10-20 cm) of the transmitting Iridium antenna (Figure 4). This was to confirm that signal reception is not compromised and to test whether extended exposure to these extreme operating conditions would lead to a progressive degradation and possibly failure of the GNSS receiver RF frontend. One year later we have observed neither serious interference nor damage.

This is quite surprising in view of earlier reports of 100 m separation between Iridium transmitters and GNSS receiver not being enough to avoid cycle slips (<https://kb.unavco.org/kb/article/iridium-gps-gnss-inteferece-from-iridium-data-transmitters-675.html>).

A possible reason for such vulnerability to interference may be the extremely (and often unnecessarily) high gain typical of the LNA in Trimble antennas. The observation that an attenuator between antenna and receiver did not help is consistent with the powerful Iridium signal saturating the LNA.

Signals can reach the receiving antenna directly from the satellite or, with a delay, after being reflected from the ground or the surrounding topography. The resulting multipath error degrades the accuracy of the final position, but the classic choke ring antenna designs with strong multipath attenuation are much too heavy, bulky and expensive for the intended applications of the INTAROS GNSS receiver.

The Novatel Pinwheel design claims to achieve comparable results by employing a different technique that allows the production of relatively small and very lightweight antennas. Figure 9 shows that multipath is generally not an issue, and we expect the typical deployment on the ice sheet to be even less affected than at this station on Qasigianniguit Glacier, which is surrounded by some higher topography. These plots further confirm the suitability of the chosen antenna and seem to compare favorably to the much more stable and expensive G-Net permanent station in Qaarsut.

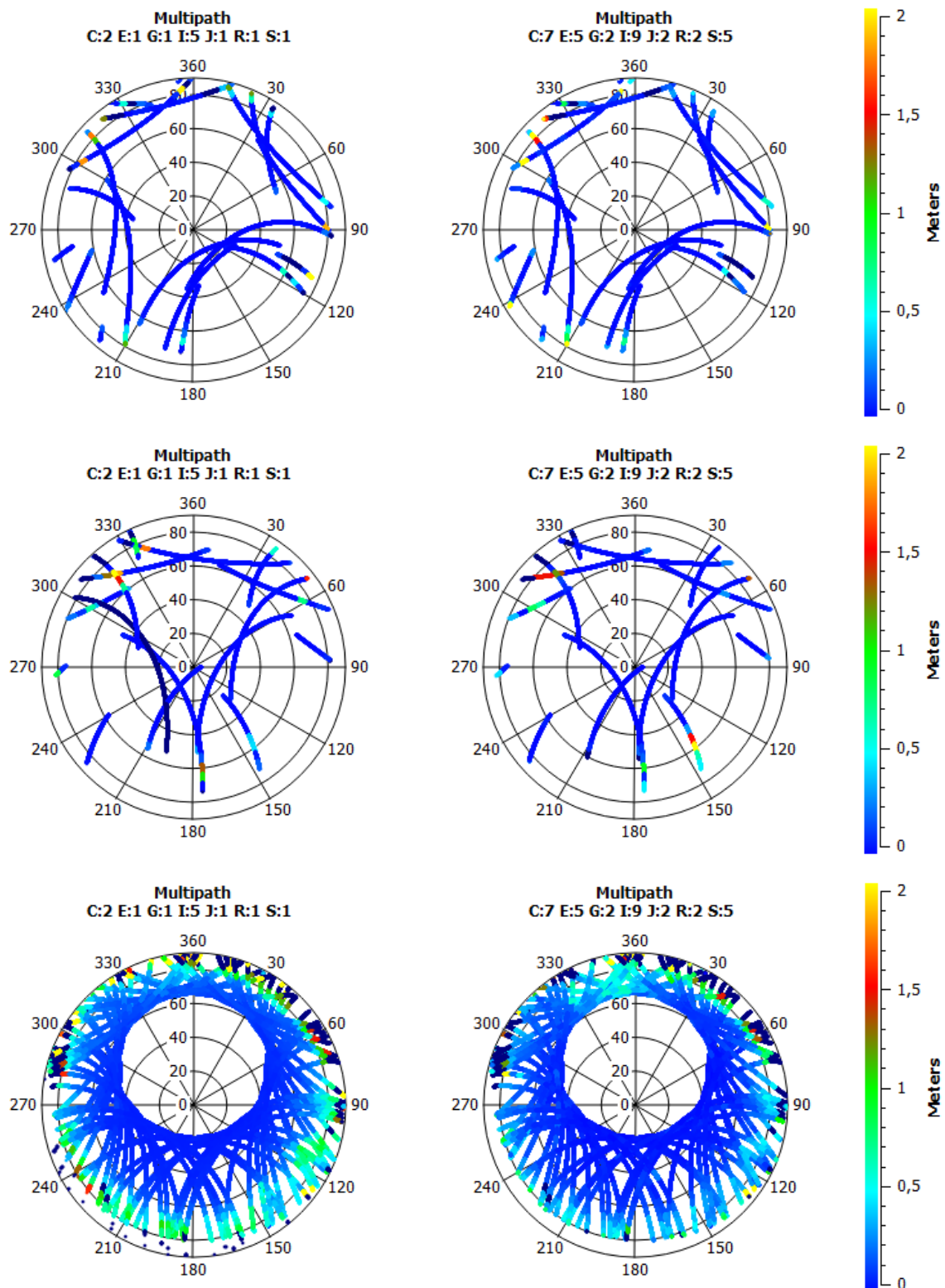


Figure 9: Plots of multipath over the same 3 hours interval for GPS (top row) and GLONASS (middle row) signals in the L1 (left) and L2 (right) frequency bands from data recorded by the INTAROS GNSS receiver on Qasigiannqut glacier. For comparison, GPS multipath over a full day from the permanent G-Net QAAR station in Qaarsut (bottom row). Higher values represent stronger signals.

Lessons learnt from the tilt and azimuth sensor deployment

The 2019-2020 test deployment on Qasigianguit Glacier close to Nuuk, Greenland unfortunately did not deliver usable data due to flashcard corruption. While the instrument is designed to communicate with the datalogger in a standard PROMICE AWS, the test deployment used a separate logging board both to avoid impacting the AWS in case of malfunctions and also because the same inputs on the datalogger are already occupied by the wires going to the legacy tilt-only sensor.

The reason for the flashcard corruption is unclear as even the earlier test files and filesystem was lost. A binary image of the card found no content whatsoever, but the card appeared functional and could be formatted successfully. Because of this apparent lack of physical damage, the most likely explanation is a sudden loss of power during a write operation, which is significantly higher than the power requirements of the tilt and azimuth sensors.

While not directly applicable to this sensor when used as intended as part of an AWS, this is an important lesson showing the need for some form of power backup when writing to a flashcard in the field, or what appears both simpler and more robust, the use of a memory solution that does not rely on complex management and allocation of flash pages as is done for wear leveling by the firmware internal to each flashcard. This would increase the chances that given the case of corruption, earlier data remains accessible. The downside is a less convenient field download of the data compared to simply swapping a flashcard.

A compromise between convenience and reliability is to include a smaller buffer memory that is written to at every measurement and only writing to the flashcard when the buffer is nearly full and the battery voltage is high. This solution has now been incorporated in the INTAROS high accuracy GNSS device.

Lessons learned from the deployment of rain gauges on ice sheet AWS

It was challenging and time consuming to have the rain gauges not integrated into the PROMICE weather stations. Therefore, we learned it saves time to integrate the precipitation recorders into existing data recording/telemetry, which is now the practice. It was also obvious that openly sharing the rainfall data accelerated the regional climate model development, underlining the need for open-access data.

2.1.3. Description of processing and analysis of the obtained data

Converting counts to snow water equivalent

The SnowFox records neutron events over a regular interval, usually one-six hours. In order to derive SWE, we first correct the raw neutron counting rate for variations in barometric pressure and solar activity, then we normalize the corrected rate to a no-snow reference counting rate. The counting rate decreases as a function of the amount of snow or SWE overlying the detector.

Table 3: Metadata for the PROMICE automatic weather station network. Latitude, longitude and elevation are derived from automated GPS measurements. P_0 and N_0 are references values for the atmospheric pressure and neutron counts for snow free conditions, respectively.

Station	Latitude (°N)	Longitude (°W)	Elevation (m a.s.l.)	P_0 (hPa)	N_0
KAN_M	67.0670	48.8355	1270	860	9000
QAS_M	61.0998	46.8330	630	930	5000
QAS_U	61.1753	46.8195	900	900	6600
TAS_A	65.7790	38.8995	890	900	6000
THU_U2	76.3903	68.1100	740	910	4500

In general, the procedure is as follows.

Correct the raw counting rate: unwanted environmental effects are eliminated by applying a correction factor $F(t)$ to the raw counting rate, N_{raw} , such that the corrected counting rate is:

$$N = F(t) \cdot N_{raw}$$

The data logger only reports the raw counting rate, so the correction must be done by the user. The overall correction factor $F(t)$ can be decomposed into correction factors for the individual processes. Currently the main correction factors account for barometric pressure (f_{bar}) and solar activity (f_{sol}). The total correction factor is thus:

$$F(t) = f_{bar} \cdot f_{sol}$$

The first of these is the barometric pressure correction factor, calculated as

$$f_{bar} = \exp[\beta \cdot (P(t) - P_0)]$$

where $P(t)$ is the barometric pressure recorded at the site [in hPa], P_0 is a fixed reference pressure [in hPa], usually taken to be an approximate long-term average for the site or calculated from the elevation and a model representation of the atmosphere. The choice of P_0 is somewhat arbitrary but must be consistent while processing the time series. β is the pressure coefficient, which at high to mid latitude can be assumed to be 0.0077 hPa^{-1} .

The second factor corrects for variations in solar activity, and is calculated as

$$f_{sol} = \frac{M_0}{M(t)}$$

where $M(t)$ is the counting rate of a neutron monitor at time t , and M_0 is the counting rate at an arbitrarily chosen reference time. (The idea is to normalize all counting rates to a single reference solar activity level; the exact reference level chosen is not important as long as the user is consistent). The factor f_{sol} is calculated on an hourly basis and reported on a Hydroinnova maintained web portal, <http://nearfld.com/reguser/solar/>. This correction factor is most accurate for high altitude sites in Europe.

Calculate the effective attenuation length, L , in water. We use the formula:

$$\frac{1}{L} = \frac{1}{L_{max}} + \left(\frac{1}{L_{min}} - \frac{1}{L_{max}} \right) \cdot \left(1 + \exp \left[-\frac{\frac{N}{N_0} - a_1}{a_2} \right] \right)^{-a_3}$$

For a SnowFox installed on the ice sheet, the recommended parameters are shown in Table 4.

Table 4: Recommended SnowFox parameters for correcting raw neutron count on ice from the manufacturer.

L _{max}	1.354x10 ² [cm]
L _{min}	1.701x10 ¹ [cm]
a1	3.071x10 ⁻¹
a2	6.330x10 ⁻²
a3	0.6029

We then calculate SWE from the exponential attenuation relationship:

$$SWE = -L \cdot \ln \left(\frac{N}{N_0} \right)$$

Here N₀ is the initial “snow free” counting rate. If L is in centimeters, then the resulting SWE will also be in centimeters.

Since PROMICE AWSs primarily set out to monitor melt and its atmospheric forcing, the stations are commonly located in high-melt regions where equipment melts out and the uneven terrain affects station stability. The ongoing cycles of freezing and thawing, and the powerful katabatic winds and winter storms are harmful to instruments. We therefore visit all stations every 1 to 4 years, balancing cost, necessity and opportunity.

SWE data product and availability

The SnowFox data is made available on a daily time resolution. The data product includes variables listed in Table 5. The data is organized in an ASCII file following Table 5. The datafiles can be accessed through the PROMICE data portal on <https://www.promice.org>.

Table 5: Short description of the variables in the data product. An updated short description version is kept as a readme_PROMICE_SWE_data.docx file in the data product download folder.

	Unit	Short description
Year	-	-
Month	-	-
Day	-	-

DayofCentury	-	-
Cor_fac_pre	-	Barometric correction factor, f_{bar}
Cor_fac_sol	-	Solar activity correction factor, f_{sol}
Uncor_count	-	Uncorrected counting rate, N_{raw}
Cor_count	-	Corrected counting rate, N .
SWE(cmWeq)	cm W. eq.	Estimated snow water equivalent of the overlying snowpack.

Examples of the SWE data product

To get a basic insight into the data product, we illustrate data from the SnowFox at the KAN_M PROMICE location in connection with AWS data.

The SnowFox records neutron events over a regular interval, usually one-six hours. In order to derive SWE, we first correct the raw neutron counting rate for variations in barometric pressure and solar activity, then normalize this corrected rate to a no-snow reference counting rate. The counting rate decreases as a function of the amount of SWE overlying the detector. As an example, we highlight the KAN_M site for the description of the SWE data. Following the above conversion procedure, we managed to convert raw counts to SWE (Figure 10).

Figure 10 illustrates the results: the top panel shows the raw and corrected counts, which is used to calculate SWE based on above conversion procedure second panel. The correction substantially smooths the variability of the measured count rate. The two bottom panels show measured snow surface height from the PROMICE AWS (we have two SR50A on our AWS setup), which are used together with the SnowFox SWE measurement to calculate the bulk snow density:

$$\rho_{snow_bulk} = \frac{SWE \cdot \rho_{water}}{H_{AWS}}$$

Starting from $N_0=9000$ (Table 3) the sensor was lying on the bare ice surface. Since the first snowfall event in mid-September 2018 the count rate dropped to around 4000 by the end 2018, where it stayed relatively constant. Figure 10 shows that with an increasing amount of snow cover through the winter season follows the evolution of the SWE measurement when the SnowFox tube is fully covered in snow.

However, calculating the bulk snow density for periods where the SnowFox tube is not fully covered in snow (SWE below 10 cm W eq.) results in much variability, which may not necessarily reflect the real changes in the snow density. Further, the snow height measurements from the PROMICE stations are recorded more than 10 meters away and may not be fully representative of the snow height over the SWE sensor during the whole winter season. The SWE changes in snow accumulation and snow melt at PROMICE sites completes the daily-weekly surface mass balance estimates for the whole year. Further, Figure 11 illustrates the problems with power in at QAS_U because of too much snow that buried our solar panel could not recharge the batteries (2019-01-06 was last measurement before burial). When the snow melted away the solar panel could recharge the batteries again and the SWE measurements started again (2019-06-16 was the first measurement after snow free solar panel).

This indicates at the QAS_U site that most of the melt from the surface in the unmeasured period refroze close to its origin because the calculated density was almost 20 % higher when comparing density at the dates 2019-01-06 and 2019-06-16, respectively. The three other sites (QAS_M, TAS_A, THU_U2) also show promising result similar to those presented in Figure 10 and Figure 11.

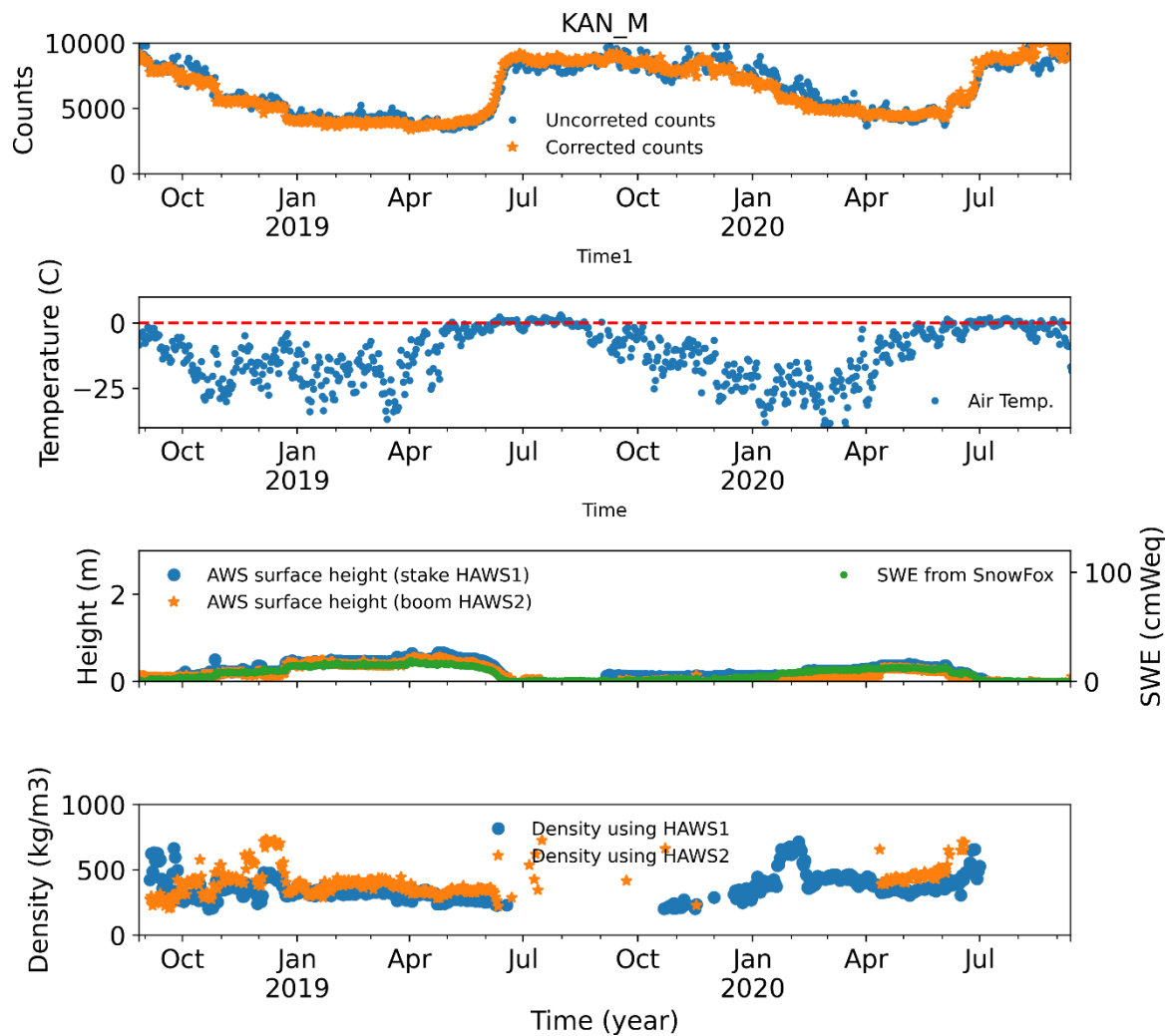


Figure 10: KAN_M site: Top panel shows the raw and corrected counts from the SWE sensor. Second panel shows observed air temperature. Third panel shows the two snow height measurements from the nearby PROMICE AWS and the calculated SWE. Fourth panel shows the calculated bulk snow density using SWE and snow height measurements.

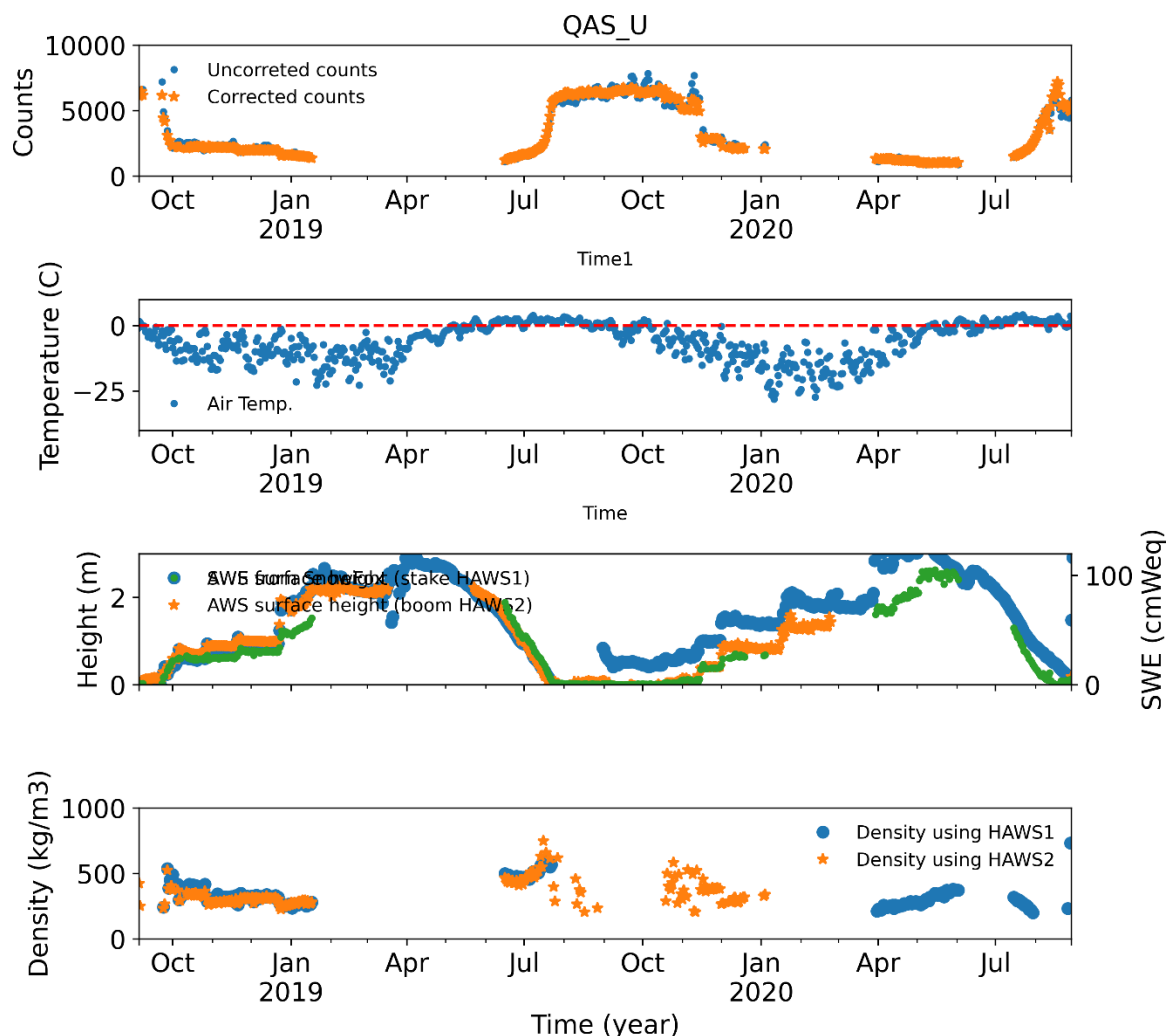


Figure 11: QAS_U site: Top panel shows the raw and corrected counts from the SWE sensor. Second panel shows observed air temperature. Third panel shows the two snow height measurements from the nearby PROMICE AWS and the calculated SWE. Fourth panel shows the calculated bulk snow density using SWE and snow height measurements.

As soon as the processed data has been properly quality controlled and validated, we will distribute the data on the PROMICE data portal.

We plan to do adjustments to the system so that it measures for a longer period of time before sensor and datalogger goes into powersave mode. The SnowFox snow water equivalent (SWE) measurements will still be kept as separately systems alongside the PROMICE station in order not to jeopardize the core station operation. Eventually, the SnowFox will be integrated in the standard station setup and established at all the stations where these parameters are relevant.

Processing and analysis of the high accuracy GNSS positioning data

The GNSS code and carrier phase observables recorded for the GPS, GLONASS and Galileo constellations on frequency bands L1, L2 and L5 were recorded locally on a flashcard, together with Doppler and SNR estimates.

Postprocessing was carried out in PPP (precise post processing) mode using readily available open-source software, primarily RTKLib, precise orbit and clock data downloaded from IGS, and standard corrections as for tidal effects as required for this type of applications. The output from the postprocessing is then summarized and plotted using tools from the scientific python stack.

Several postprocessing parameters can be optimized, such as the elevation mask used for excluding satellites low on the horizon with noisy signals. The optimal settings depend on many technical characteristics of the antenna, receiver, and site. Figure 12 shows an example of the effect of changing the elevation mask between 5 and 20 degrees, resulting in a spread of the horizontal and vertical components of the position solution in the order of 1.5 cm in the horizontal plane and 5 cm in elevation for our new instrument. The position wandering is within 3 cm both in the horizontal and vertical planes.

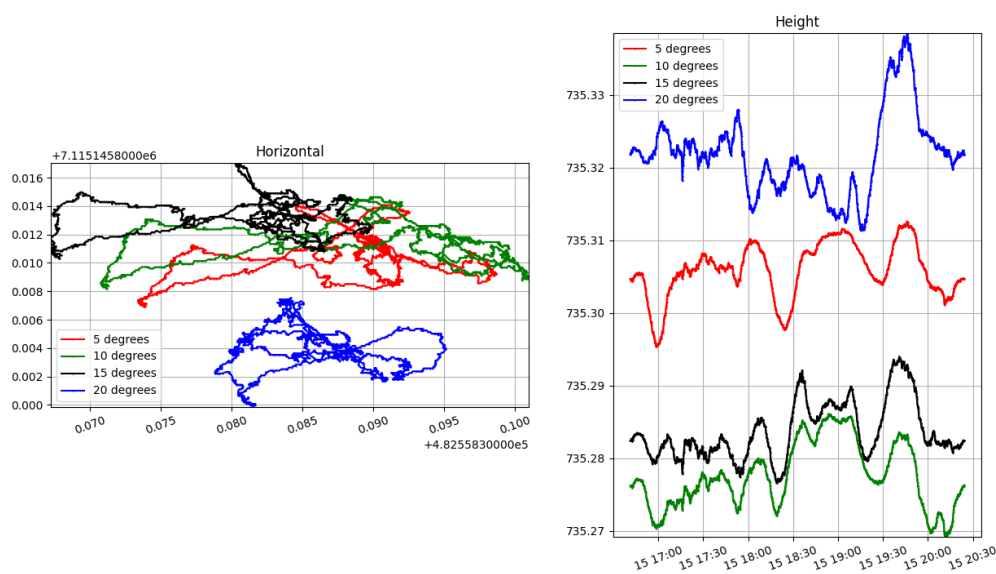


Figure 12: Effect of changing the elevation mask parameter during postprocessing of a typical 3-hours record from the new INTAROS GNSS receiver on Qasigiannquit Glacier.

Continuing our comparison with results obtained from postprocessing the much higher stability and cost installation at the permanent G-Net QAAR reference station in Qaarsut, Figure 13 shows that the new INTAROS high accuracy GNSS receiver produces a wandering of 2 to 3 times larger, but still within 1.5 cm in the horizontal plane and 3 in elevation which are very encouraging. Due to very slow ice flow in the lower part of Qasigiannquit Glacier, the position of the antenna can be assumed to be stable during the 3 hours shown in Figure 13.

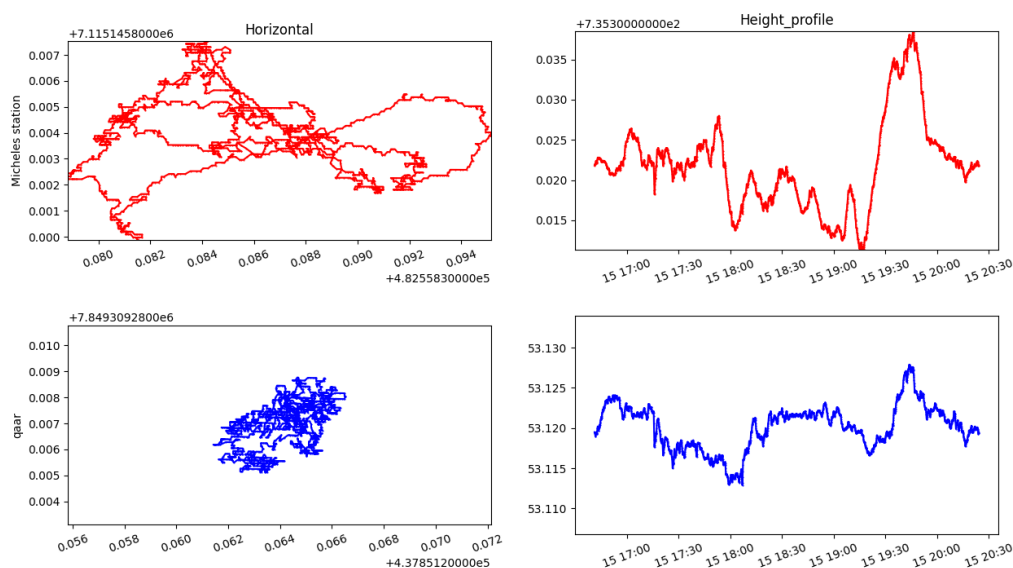


Figure 13: Comparing horizontal (left) and elevation (right) wandering over 3 hours of observations at the new INTAROS GNSS receiver on Qasigiannquit Glacier (top) and at the G-Net QAAR permanent reference station (bottom). The elevation mask is set to 20 degrees.

The 2019-2020 deployment took place at an AWS that is equipped with an ablation meter that uses a pressure transducer to measure how much glacier ice melts during the summer season. Because ice flow is extremely slow at this site (less than 30 cm northward between March and August 2020), the vertical lowering of the AWS tripod and the GNSS antenna mounted on it can be expected to be very close to surface ablation, which is indeed the case as shown in Figure 14.

It is important to remember that the GNSS antenna in this case is not installed on a high stability monument as is the case with e.g. the G-Net permanent reference stations. The AWS tripod is an aluminum frame tensioned by guy wires and can deform elastically to some degree, primarily under the loading of snow and wind. Furthermore, it is standing freely on the glacier surface, so it is subject to tilting due to differential ablation and the irregularity of the glacier surface.

This means that the occasional displacements larger than the error bars, and the apparent reversal of movement from northward to southward of the last 5 positions are most likely due to the tripod slightly adjusting to the melting glacier surface.

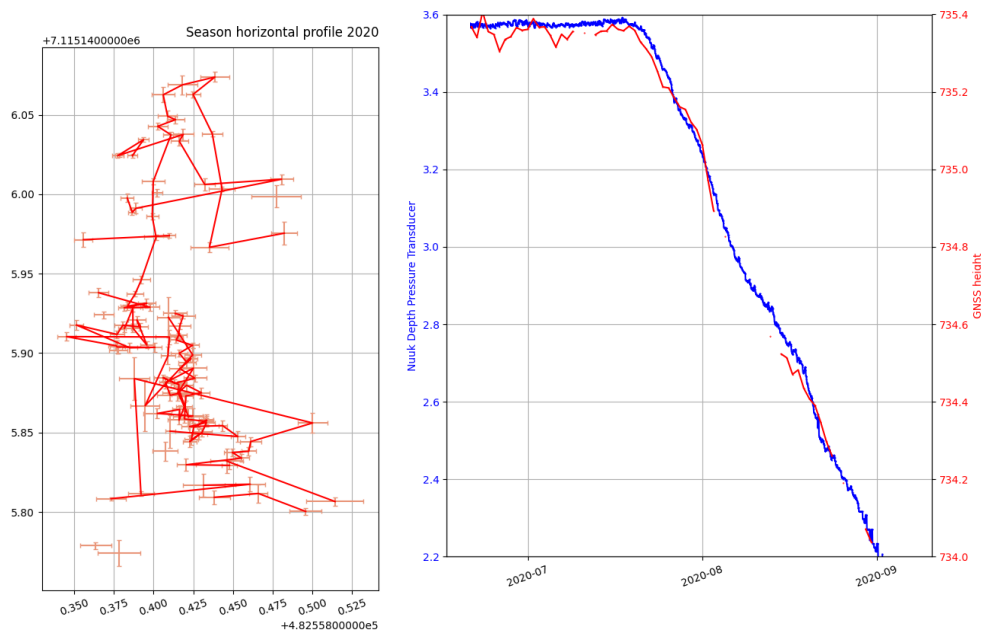


Figure 14: Horizontal displacement from March to August (left) including error bars, and vertical displacement (right) comparing ablation as measured by the pressure transducer and surface lowering from the new GNSS instrument. Horizontal coordinates are in meters referred to the UTM coordinate system, vertical units are meters above the WGS84 ellipsoid for the GNSS height and a local instrument datum for the pressure transducer.

Processing and analysis of tilt and azimuth data

The tilt and azimuth instruments developed in INTAROS internally runs a number of self-checks to verify that the sensors are producing reasonable measurements and the error codes can be read through the SDI-12 interface and should be used for quality control. The processing of the output data is meant to be the same as currently implemented operationally for the PROMICE AWS as a direct replacement for the current tilt-only sensor. The additional azimuth information can simply replace the constant azimuth as measured at AWS maintenance time.

The data loss during the 2019-2020 test deployment season means that no further analysis could be conducted using actual field data from Greenland. A new field deployment will start at Chamberlin Glacier, Disko Island, within the collaboration with the GEM (Greenland Ecosystem Monitoring) GlacioBasis Programme.

Processing and analysis of rain gauge data – undercatch correction

Given that the TR-525I gauge has a cylindrical shape, we apply an undercatch correction for an unshielded Hellmann-type precipitation gauge under mixed (solid and liquid) precipitation conditions. We adopt a catch efficiency (k) correction after (Yang et al., 1999):

$$k = 100 / (100.00 - 4.37U + 0.35U^2)$$

where wind speed (U) has units of m s^{-1} and is at gauge height. We use the PROMICE AWS hourly average observations interpolated linearly in time to each TR-525I data that are recorded as events logged with a precision of seconds. U . The correction was implemented using daily averages in the $0 \leq U \leq 6.5 \text{ m s}^{-1}$. We assume the equation is valid for hourly wind speeds (the (Yang et al., 1999) implementation is for daily averages) and when wind speed exceeds 6.5 m s^{-1} which for rain events is 7-12% of cases.

While Yang et al. (1999) conclude that wetting and evaporation losses correspond with a measurement error of less than 0.1 mm, which is below the 0.2 mm resolution of the TR-525I gauge measurement, we account for trace precipitation by setting the lowest possible rainfall correction to 1.01.

2.1.4. Accessibility of the obtained data sets and repositories used

SWE data sets from the SnowFox instruments

The SnowFox datasets are available through the PROMICE data portal. The data portal uses an open-source web application called “dataverse”. The PROMICE dataverse shares real-time, derived and quality-checked data from a variety of in-house and external data sources. The PROMICE dataverse should handle researchers, data authors, publishers, data distributors, and affiliated institutions in a more appropriate and systematic way, so that all receive appropriate credit via data citation with a persistent identifier. Data users also have the option of using the Application Programming Interface (API) to make automated data download scripts “computer talking to computer” for the convenience of often updated data product. In connection with the dataset, we associate a Github repository for user dialog and continued optimization of the data product (GitHub link).

The data is accessible here: <https://doi.org/10.22008/FK2/B5KVJV>

Availability of the high accuracy GNSS positioning data

The data collected in 2019 and 2020 are primarily of interest as a demonstration of the technical performance of the system and helped in refining the design. As such, they are available upon request but are not being archived as a science-ready dataset on any public repository. The data that will be acquired from 2021 will have primarily a scientific purpose and will be made publicly available through the GEUS dataverse portal.

Accessibility of the tilt and azimuth data sets

The 2019-2020 test deployment on Qasigiannuit Glacier close to Nuuk, Greenland did not deliver usable data due to corruption of the flashcard. When successfully implemented, the data sets will be available along with all other PROMICE data from the AWS network on the Greenland ice sheet.

Access to rain gauge data sets

An open access 'dataverse' is in preparation and will include the following DOI permalink:
Box, Jason, 2021, "GEUS rainfall observations from Greenland ice sheet locations",
<https://doi.org/10.22008/FK2/MOHLI3>, GEUS Dataverse.

2.1.5. Future plans for operation of the observing system, including data provision

Future plans for SWE observations on the Greenland ice sheet

Winter snowfall and the associated mass or snow water equivalent (SWE) of a snowpack in Greenland is a major mass budget term. The new data quantifies how much mass that accumulates as snow during the winter season on the Greenland ice sheet. The plan is to fully implement and integrate the SnowFox sensor in the automatic weather station system operated by PROMICE. The measurements from the SnowFox sensor fully complement the other instruments to monitor changes in the daily surface mass balance. All future measurement will likely be integrated into the PROMICE data product when the power issue of the present system is solved. The data achieved through this project will remain accessible here: <https://doi.org/10.22008/FK2/B5KVJV>. Any future data assimilation will be quality checked and processed following the above-mentioned data set production chain. The future updated datasets will be accessible through the same data portal.

Future use of high accuracy GNSS positioning on non-stationary automatic weather stations

The GNSS device is fit for application both as a standalone unit for applications such as monitoring of ice velocities and as a component of larger systems such as the PROMICE automatic weather stations (AWS). The very low power consumption allows implementation anywhere year-round in the Arctic. The data quality is very satisfactory, considering the much lower price, weight, size and power consumption. This has to be compared to permanent GNSS installation, such as those part of GNet, which are impossible to deploy on ice. The logistics requirements, both for installation and maintenance, are no different than a PROMICE AWS for a standalone GNSS unit and can easily be installed at the same time of the AWS. Costs-wise, after the initial purchase cost, the only operating costs are for data transmission via satellite and, if desired and available on the market, the subscription to L-band PPP augmentation services.

There are four promising avenues for further development of the GNSS high accuracy receiver

- The first is adding a terrestrial data link capability, so that differential processing over baselines of in the order of some kilometers becomes possible. This goes for real-time applications. This also opens for "a moving base" processing, where the 3d vector between the base and rover is monitored accurately independent on the movement of the base station.
- The second is a drop-in compatible carrier board to replace the current dual/triple frequency OEM GNSS receiver with lower cost dual frequency modules. These have come to the market during the recent years, for use in more cost-sensitive applications where a slightly lower positional accuracy can be accepted.

- The third is to develop a more tailored data processing workflow that takes full advantage of the very constrained dynamics of a receiver moving downglacier, in order to obtain the highest possible positional accuracy from the limited amount of data that can be easily transmitted via Iridium. Logging frequency could be reduced to 60 seconds instead of 5 seconds, observations could be reduced to GPS only and by raising the elevation mask to 10 deg. This leads to a potential data reduction of up to 95% of the data currently logged during 2020, with only a limited loss of position accuracy.
- The fourth is to explore the use of passive antennas and the impact on tracking and position accuracy under arctic conditions. This is also related to ionospheric scintillations as well as multipath reflections from Ice, which has not been explored in this project. This could be done using a dual antenna input board, where both an active and a passive antenna are connected. In this case the comparison would be easier since the receiver clock would be identical for the two datasets.

Regarding the planned future uses for the new INTAROS high accuracy GNSS receiver, these are listed below:

- Measure accurate position, especially elevation, of PROMICE and Glaciobasis AWS to make their meteorological records suitable for operational numerical weather prediction
- Monitor ice velocity for calibration and validation of SAR surface velocity grids produced by PROMICE using Sentinel-1 data
- Estimate snow depth from GNSS reflectometry
- Instrument strain networks to investigate dynamic thinning at key sites on the GrIS
- Estimate firn compaction rates in the accumulation zone of the GrIS.
- A slightly modified version of the instrument will be installed during 2021 for investigating landslides risk at two sites in Greenland

These planned applications address the Glaciers, Ice Sheets and Ice Shelves, Permafrost, and Snow ECVs.

Future plans and data provision of radiometer tilt and azimuth data

The raw and processed data once available will be stored in the PROMICE database at GEUS and disseminated through the promice.dk website. This type of data will become a regular part of the transmitted near real-time data stream from the PROMICE and GC-Net weather stations.

Future plans for deployment and operation of the rain gauges

The observing system is being expanded by adding locations (Table 6) and integrating the measurements into existing recording/data telemetry sites.

Table 6: Greenland precipitation observations through this activity.

site	latitude, deg. N	longitude, deg.	elevation, m	date of first recording
QAS L-16	60.951	-46.938	20	6/9/2018
QAS_L	61.031	-46.849	271	8/10/2016
QAS_M	61.099	-46.833	621	8/10/2016
QAS_U	61.174	-46.820	893	8/30/2018
KAN_L	67.095	-49.953	664	8/31/2017
KAN_B	67.125	-50.183	350	4/18/2016
Narsaq	60.917	-46.059	25	7/5/2016
QAS_U_luft	61.174	-46.820	893	8/30/2018
QAS_B	61.076	-46.793	553	7/4/2020
JAR	69.498	-49.682	960	8/7/2020
SWC	69.554	-49.371	1219	8/8/2020

The proliferation of precipitation sites is through three actively funded projects:

1. PROMICE
2. GC-Net
 - a. Currently, two PROMICE-type AWS at SWC and JAR now host a Lufft WS401-UMB rain gauges (Table 6).
3. Greenland Integrated Observing System (GIOS)
 - a. <https://gios.org/>
 - b. Via GIOS, the installation/maintenance of two Greenland nunatak-based precipitation observatories is planned. Figure 15 illustrates an already-installed site at QAS_B (Table 6).

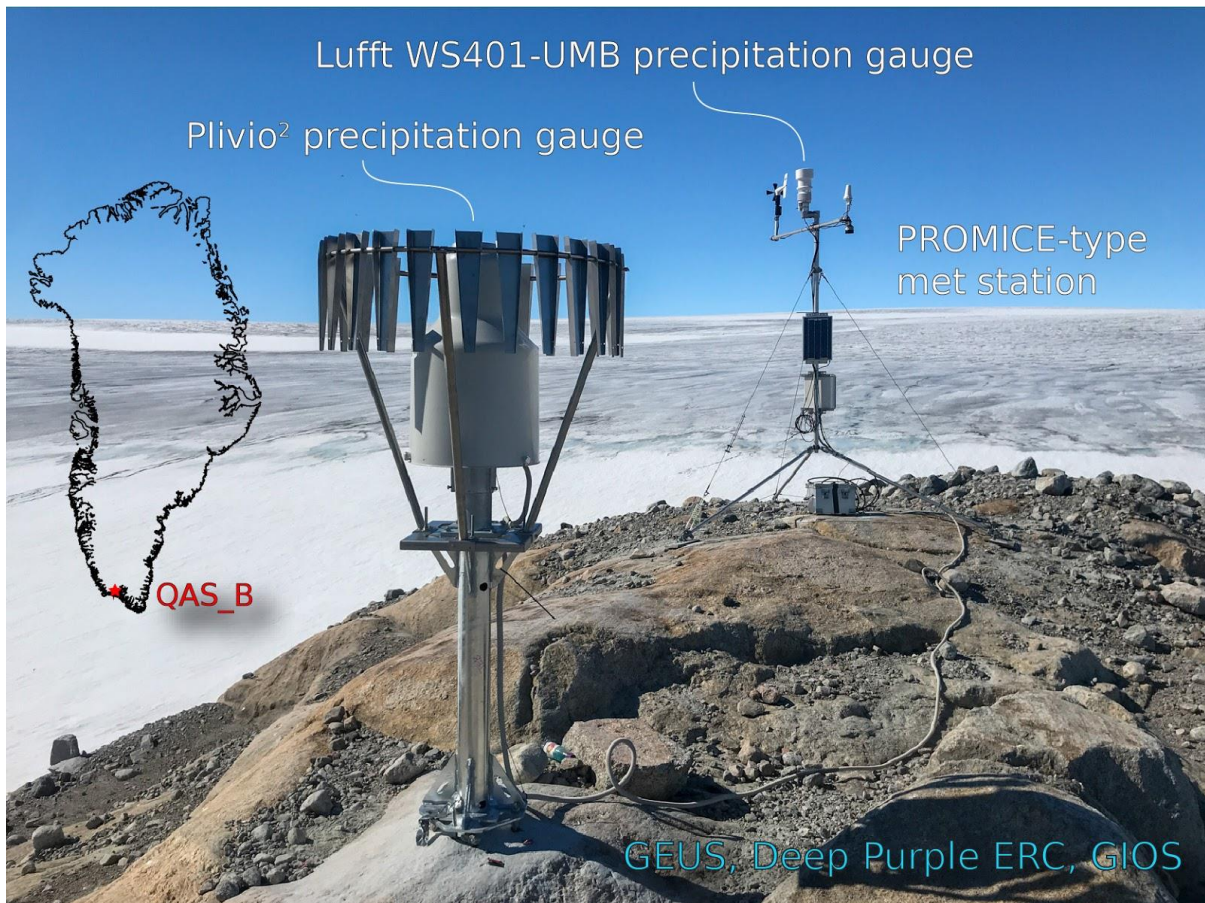


Figure 15: New QAS_B precipitation and climate observatory on a Greenland nunatak (61.076 N, 46.793 W, 553 m a.s.l.), installed July 4, 2020.

2.2. AU

Contributors: Mikael Sejr and Johnna Holding

2.2.1. Results of the final implementation of the observing system

To improve the acquisition of seasonal ocean data in the marine component of the Greenland Ecosystem Monitoring program in Young Sound, NE Greenland, two new instruments were tested. At the existing mooring array in the central fjord, a new instrument was added at 20 m depth. A RBR Maestro³ CTD with sensors for conductivity, pressure and temperature was fitted with the following additional sensors: fluorescence (Turner Cyclops), turbidity (Seapoint), oxygen (RBRcoda ODO) and Photosynthetic Active Radiation (Licor Spherical 193SA).

To resolve local variation in the fjord and specifically to measure the impact from glacial runoff from the Greenland Ice sheet a new mooring in the inner fjord was established and fitted with a single instrument at 10 m; a RBRConcerto³ CTD with similar sensors for Photosynthetic Active Radiation and turbidity.

To ensure continuous data could be collected two instruments of each kind was purchased to enable us to have one in active rotation while the other is available for service and calibration. The two instruments were deployed in August 2018 and retrieved one year later and replaced with new instruments. Two full years of data is thus available while a third year will be available upon successful retrieval in August 2021.

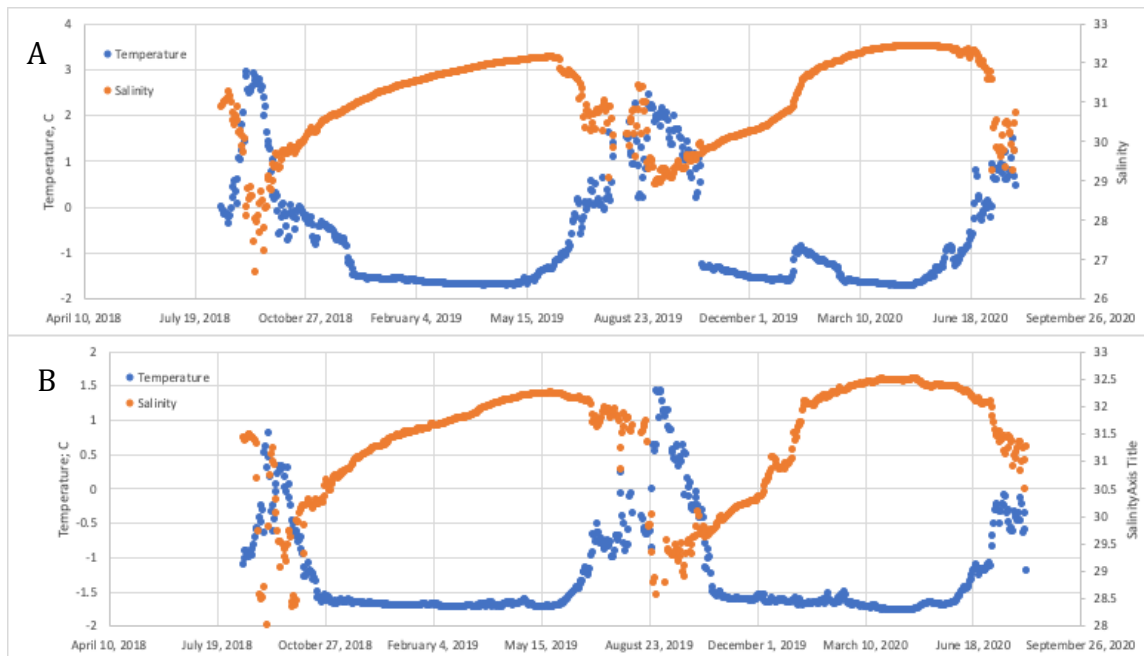


Figure 16: Daily average temperature and salinity from two instruments in Young Sound. A. Data from 10 m depth in inner Young Sound and B. from 18 m depth in outer Young Sound.

2.2.2. Lessons learned and technology challenges identified during the project

The aim was to reliably collect precise and continuous measurements in this NE Greenland fjord. Because the area is only visited once a year, we chose proven off-the shelf solutions. So far, the instruments have delivered as expected and have presented few challenges. The major challenge has been to locate regions in the fjord where the risk of ice bergs is as low as possible. At present, we are not able to assess the precision of the measurements from each sensor other than the information given by the company on calibration accuracy and estimated drift.

2.2.3. Description of processing and analysis of the obtained data

Data is collected at 2 Hz by the sensors but due to battery capacity limitations instruments were set to collect data every hour and averaging over a 5 sec sampling period. For overview of data, daily averages were calculated (Figure 16). For PAR values, all instruments displayed an off-set of about 4 $\mu\text{Mol}/\text{m}^2/\text{s}$ resulting in negative light values in winter, which was corrected for.

Table 7: Overview of parameters and sensor for the two instruments.



Parameter	Sensor	Units
RBR Maestro³		
Conductivity	Marine CT	mS/cm
Temperature	Marine CT	°C
Pressure	RBR	dbar
Chlorophyll a	Turner Cyclops	µg/L
PAR	Licor PAR	µMol/m ² /s
Turbidity	Seapoint	NTU
O ₂ concentration	RBRcoda	µmol/L
RBR Concerto³		
Conductivity	Marine CT	mS/cm
Temperature	Marine CT	°C
Pressure	RBR	dbar
PAR	Licor PAR	µMol/m ² /s
Turbidity	Seapoint	NTU

2.2.4. Accessibility of the obtained data sets and repositories used

The final data set comprised of data from two instruments from August 2018 to August 2021 will be made available at the GEM public online database as well as on our public community site; Greenland Marine Ecosystem Community Data repository on Zenodo (<https://zenodo.org/communities/greenmardata/?page=1&size=20>). Links to both repositories will also be available from the INTAROS Arctic Data base portal.

2.2.5. Future plans for operation of the observing system, including data provision

It is the plan to continue operating, servicing and calibrating the instruments, to keep them as an integrated long-term component in the GEM program. As with other data collected in the programme, it will be made publicly available at the GEM data repository.

2.3. FMI

Contributors: Roberta Pirazzini, Teijo Arponen, Antti Aarva

2.3.1. Results of the final implementation of the laboratory facilities to characterize optical sensors - upgrade of the PROMICE pyranometers through laboratory characterization

The total uncertainty in the incoming and reflected shortwave radiative fluxes measured with pyranometers results from the sum of several error sources. Some of them consist of instrumental errors, some others are caused by the installation setup (tilting, shadows, obstruction of the field of view of the sensors), and some by the unknown surface tilting or presence of anisotropic 3D features at the surface such as sastrugi, crevasses, waves (Pirazzini, 2004).

We aimed here to reduce the measurement uncertainty of the pyranometers used in the PROMICE network in Greenland by characterizing their thermal and angular response, providing instrument-specific corrections that can be applied operationally to minimize the instrumental errors. In the PROMICE network, the broadband radiation fluxes are measured with Kipp and Zonen CNR1 and CNR4 net radiometers (Figure 17).

In this task we characterized the upward and downward looking pyranometers belonging to three CNR1 and one CNR4, for a total of 8 sensors. The work was carried out in the FMI optical laboratory, which was equipped with a thermal chamber (for the thermal characterization of the sensors) and an automatized rotation stage (for the angular characterization of the sensors) and includes the reference lamps and the optomechanics components needed to calibrate pyranometers and spectro-radiometers following standard protocols (Kratzemberg et al., 2006).

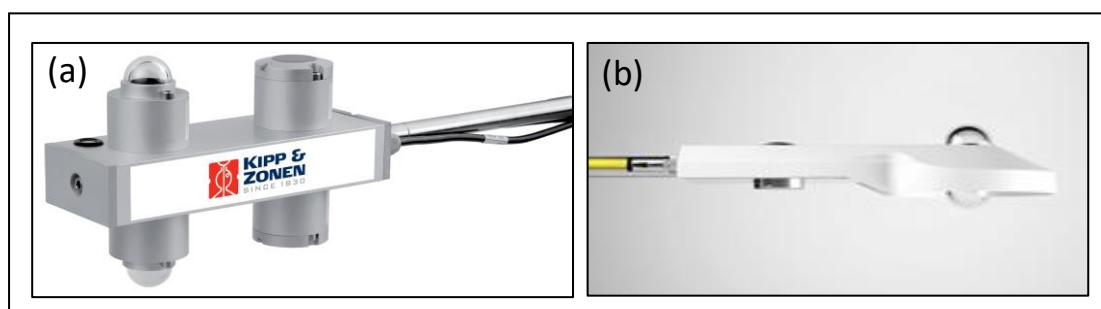


Figure 17: Kipp and Zonen net radiometers CNR1 (a) and CNR4 (b).

This is pilot work intended to demonstrate the benefits of the reduced data uncertainty, with the aim of opening the path for a systematic characterization of the pyranometers installed in all the PROMICE stations.

Thermal characterization

The manufacturer provides a generic characterization of the thermal response of the CNR1 and CNR4 pyranometers, stating that the temperature dependence of their sensitivity is $\pm 6\%$ and $< 4\%$, for the CNR1 and CNR4, respectively, in the temperature range between $-10\text{ }^{\circ}\text{C}$ and $+40\text{ }^{\circ}\text{C}$. Here we wanted to characterize this temperature dependence for each individual instrument down to $-30\text{ }^{\circ}\text{C}$, which is not an uncommon temperature during spring in the Greenland ablation area, and we provide for each instrument an equation that corrects the drift as a function of the temperature, thus reducing this source of uncertainty.

By placing the CNR1 and CNR4 net-radiometers inside a thermally controlled chamber (Figure 18), we measured their pyranometer outputs every $10\text{ }^{\circ}\text{C}$ intervals in the range between $-30\text{ }^{\circ}\text{C}$ and $+30\text{ }^{\circ}\text{C}$. We first measured the zero offset of the pyranometers at the selected temperatures, and then their response to a pre-burned 250W lamp located outside the chamber (Figure 18).

As described in detail in Section 2.3.3, the response of the pyranometers at different temperatures varied a lot among sensors, showing in some cases also opposite dependencies. However, the response was consistent among the pair of sensors installed in the same instrument. The output of some instruments was more sensitive to the temperature than the output of others: for the most sensitive pyranometers, the derived equations to correct for the thermal drift will increase the accuracy of the broadband irradiance by several W/m^2 .

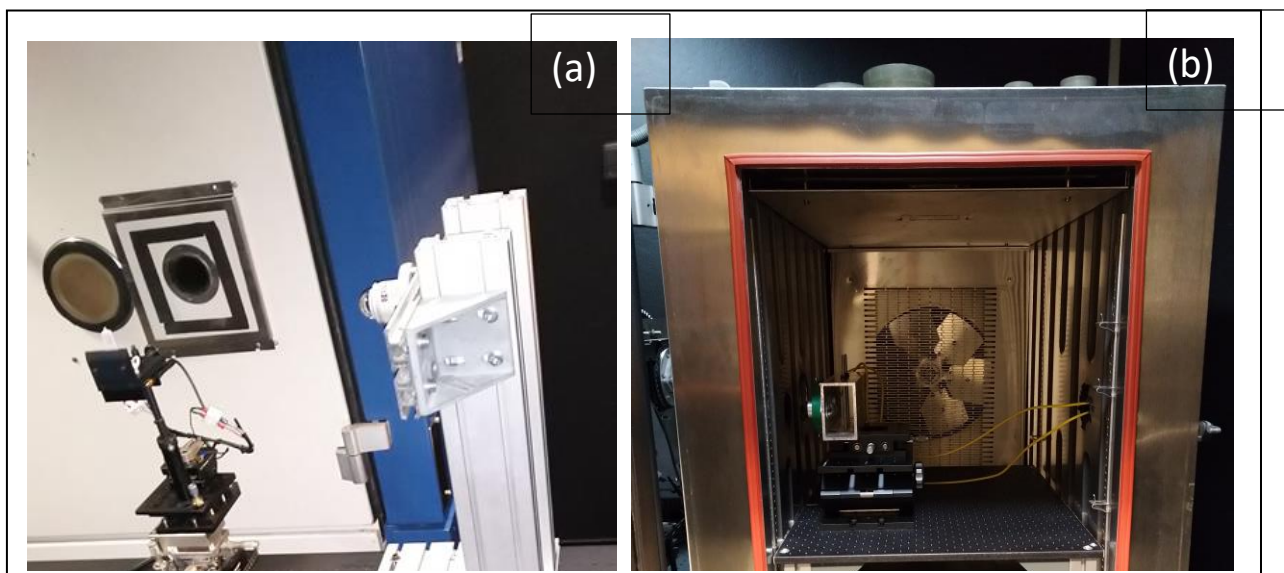


Figure 18: Laboratory setup for the thermal characterization of the CNR1 and CNR4 pyranometers: detail of the thermal chamber with the entrance hole for the light covered by a quartz glass, the lamp in front of it, and the reference pyranometer placed at the same distance from the lamp as the CNR1/CNR4 pyranometer measuring inside the chamber (a). The interior of the thermal chamber is illustrated in (b).

Angular characterization

According to the manufacturer, the deviation of the directional response from the perfect cosine response varies among the CNR1 and CNR4 pyranometers in a rather wide range, whose standard deviation is $\pm 2.5\%$ at the zenith angle of 0° - 30° and rises to $\pm 15\%$ at the zenith angle of 80° . In sunny conditions, when direct sunlight hits the upward looking pyranometer, this deviation causes an error of corresponding magnitude in the measured irradiance. The error range shifts between $\pm 4\%$ and $\pm 15\%$ at the latitudes of the PROMISE stations (between 61 and 80 N) where the yearly maximum solar zenith angle ranges between 50 and 58 degrees.

As each instrument has an individual angular response, a first step to correct for this error is the characterization of the deviation from the perfect cosine response for each pyranometer. Once this deviation is measured, it should be applied to calculate the fraction of direct sunlight that has been underestimated/overestimated by the pyranometer. This calculation requires the measurement or modelling of the ratio between direct and diffuse incoming irradiance. Thus, for the automatization of the correction procedure, look up tables of the ratio between direct and diffuse incoming radiation for different solar zenith angles and for different values of the measured irradiance need to be generated.

In the FMI optical lab, we measured the deviation from the perfect cosine response of each of the 4 pairs of pyranometers utilizing a motorized dual axis rotation stage (Figure 19).

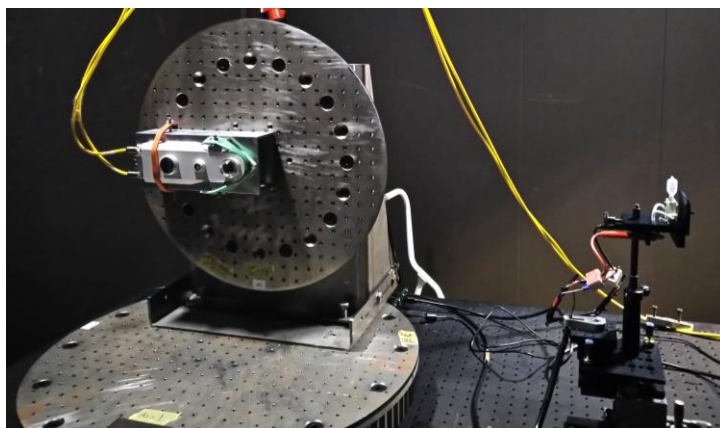


Figure 19: Measurement setup for the angular characterization of the CNR1/CNR4 pyranometers: motorized dual axis rotation stage with a CNR1 attached on the vertical rotation plate, and pre-burned 250 W lamp on the right.

The results (described in detail in Sect 2.3.3) showed the peculiar angular response of the individual pyranometers, indeed spanning in the range given by the manufacturer. All the tested instruments showed increasing underestimation of the irradiance with the increasing solar zenith angle, implying that clear-sky irradiances measured with these instruments are biased low (in some cases the negative bias is larger than 12% at 80° zenith angle) if no angular correction is applied.

2.3.2. Lessons learned and technology challenges identified during the project

The laboratory facility developed in FMI to characterize the thermal and angular response of pyranometers (and of whatever other optical device including spectral radiometers) proved able to characterize the angular and thermal response of the pyranometers of four net-radiometers employed in the PROMICE network.

The obtained results highlight the variability of responses among the sensors. This points to the need of thermal and angular characterization of the pyranometers, especially those employed in operational networks, as it can improve the accuracy of the measured broadband irradiance by several W/m², with significant implications for Greenland surface mass and energy budget estimations and validation of models and remote sensing products. We are not aware of other existing efforts to characterize the thermal and angular response of operational pyranometers: we realize that facilities such as the one equipped in FMI are rare and require significant investment and expertise to run and maintain it. The collaboration between GEUS and FMI initiated within INTAROS should therefore continue, and possibly involve also the Kipp and Zonen manufacturer, to capitalize on the experience gained in this project for the benefit of the entire community involved in radiation measurements.

2.3.3. Description of processing and derivation of the correction equations

In this section, a detailed description of the laboratory procedure and data processing done to characterize the pyranometers of the CNR1 and CNR4 net-radiometers is provided.

Thermal characterization

We studied the drift of the sensor's sensitivity with temperature using a thermally controlled chamber, equipped with a quartz glass window that is transparent to the light in the wavelength range measured by pyranometers (300-2800 nm). The chamber is ventilated both inside and outside, with air blowing toward the external side of the quartz glass to prevent condensation.

The instruments were placed inside the chamber to measure the irradiance generated by a pre-burned 250W lamp located outside the chamber (Figure 18). The measurements were performed at seven temperatures (-30 °C, -20 °C, -10 °C, 0 °C, 10 °C, 20 °C, 30 °C): after the chamber stabilized to the desired temperature (it took about one hour), data were recorded for about 10 minutes and averaged over this time interval. The output of the lamp was monitored by a reference pyranometer (Kipp and Zonen CM6) located at the same distance from the lamp as the CNR1/CNR4 pyranometer measuring inside the chamber. Before measuring the thermal response of the pyranometers, the zero offset of each instrument was characterized.

Zero offset of pyranometers

The manufacturer provides the zero offset of the CNR1 and CNR4 pyranometers due to thermal radiation emitted by the dome to the colder atmosphere during night (zero offset A) and to temperature changes in the surrounding air (zero offset B). Zero offset A is lower and equal to $+15 \text{ W/m}^2$ for CNR4 and CNR1, respectively, while zero offset B for 5K/h temperature change is lower than 3 W/m^2 and $\pm 4 \text{ W/m}^2$ for CNR4 and CNR1, respectively. In case of ventilated sensors, the manufacturer reported a zero offset B $< 1 \text{ W/m}^2$ for CNR4 pyranometers. In our experiments, we measured the zero offset B of the pyranometers when their pt100 thermally stabilized ($\Delta T < 0.01 \text{ }^\circ\text{C}$) for at least 10 minutes to the wanted temperatures, to account for this eventual offset in the calculation of the temperature dependence of the output of pyranometers.

The thermal stabilization of the Pt100 was reached after the chamber had remained at the chosen temperature for at least 30 minutes. During the zero offset measurements, the dome of the pyranometers was covered by a cup. When the chamber reached the thermal equilibrium, its temperature was maintained through a 1-minute cycle of 30 seconds cooling/warming followed by 30 seconds without cooling/warming, with an oscillation of $\pm 0.01 \text{ }^\circ\text{C}$. Hence, also the output of the pyranometers oscillated following the cyclical temperature changes of the chamber.

Figure 20 illustrates the 10-minute averaged zero offset voltage of the four pairs of tested pyranometers at the seven temperatures of the chamber, as well as its standard deviation resulting from the described oscillation. The zero offset voltages ranged from $-5 \text{ } \mu\text{V}$ to $+12 \text{ } \mu\text{V}$. To convert the voltage output V into irradiance E , the equation $E=V/C$ is applied, where C is the calibration factor (sensitivity). For the upward and downward looking pyranometers of the CNR1, the Kipp and Zonen manufacturer provides identical calibration factors, made equal with shunt and series resistors. On the contrary, the CNR4 pyranometers have individual calibration factors. As calibration factors are of the order of $\sim 10 \text{ } \mu\text{V/W/m}^2$, the zero offsets irradiances obtained from the data in Figure 20 are below or around 1 W/m^2 in the entire temperature range between $-30 \text{ }^\circ\text{C}$ and $+30 \text{ }^\circ\text{C}$, confirming the estimation for zero offset B made by the manufacturer in case of ventilated instruments.

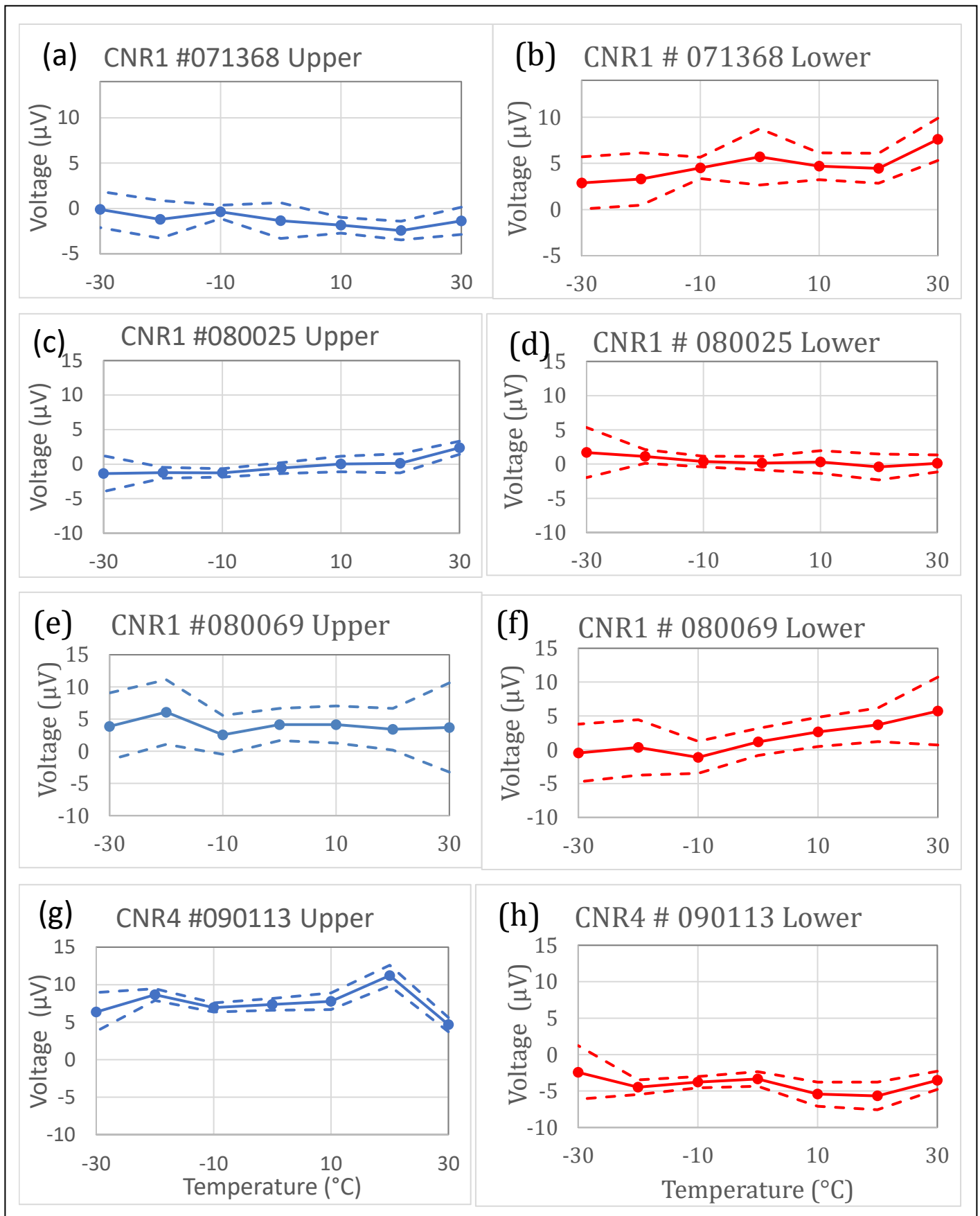


Figure 20: Voltage output of pyranometers (with the dome obscured) corresponding to the zero offset B for the considered temperatures.

Sensitivity drift in the temperature range between -30 °C and +30 °C

The CNR1/CNR4 placed inside the thermal chamber was kept for 45 minutes at the selected temperatures to enable the body of the pyranometers to reach the thermal equilibrium. In some case more time would have been needed. The voltage output was then recorded for 10 minutes and averaged out. The standard deviation of the average is associated to the cyclical oscillations of the chamber temperature and to the slight drift of the temperature of the CNR1/CNR4 body when it did not fully reach the equilibrium. The standard deviation of the temperature recorded by the Pt100 thermistor located in the body of the CNR1/CNR4 during the 10 minutes of data recording was in any case very small, $\leq 0.1^{\circ}\text{C}$. The 10-minute averaged outputs of the pyranometers and their standard deviations (σ_V) for the considered temperatures are shown in Figure 21.

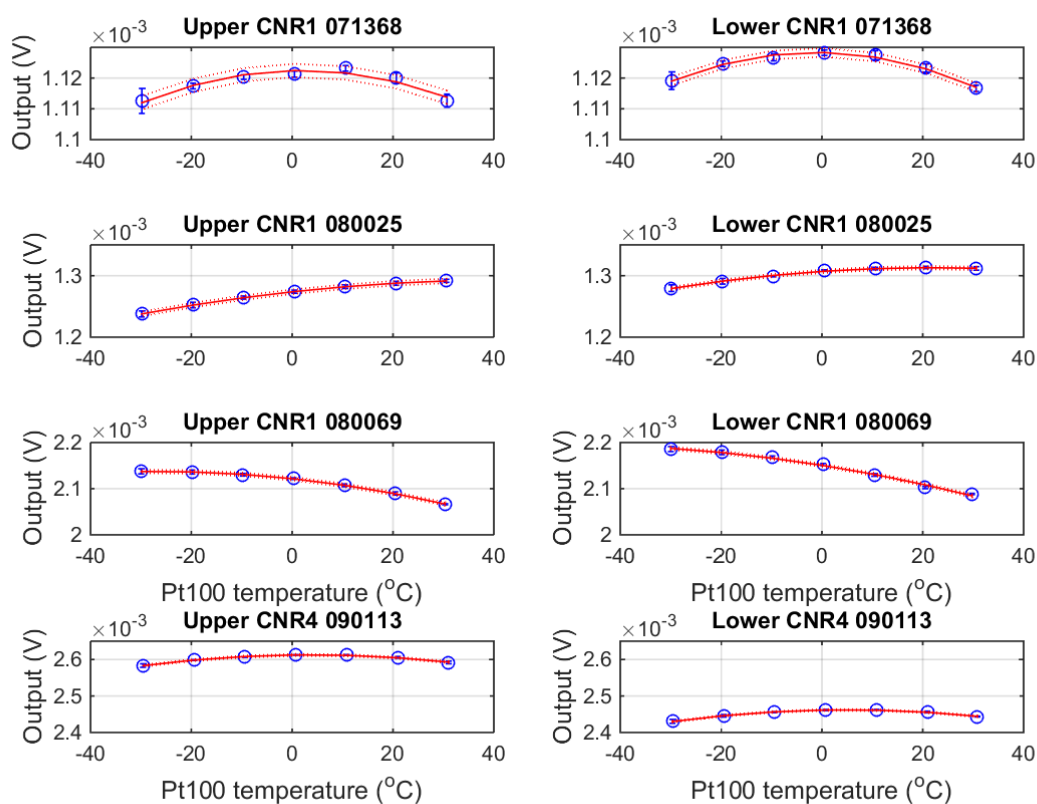


Figure 21: Averaged voltage outputs of pyranometers (blue circles) at the tested temperatures and fitted second order polynomial (red curve) applied to correct the voltage drift. The vertical blue bars correspond to the standard deviation σ_V of the voltage averages, and the red dotted lines represent the estimated error associated to the correction equation ($\pm RMSE_{corr}$, Eq. (3)).

With constant irradiance, the response of the pyranometers at different temperatures varied a lot among sensors, showing in some cases also opposite dependencies (Figure 21). However, the response was consistent among the pair of sensors installed in the same instrument.

The drift of the pyranometers output with temperature shown in Figure 21 can be approximated with a second order polynomial. We derive a correction equation that expresses the voltage output as a function of the Pt100 temperature T and of the voltage V_0 measured at the calibration temperature $T_0 = 22^\circ\text{C} \pm 2$:

$$V(T, V_0) = V_0 + a + b(T - T_0) + c(T - T_0)^2 \quad (1)$$

Hence, the conversion of the voltages to irradiances can be done applying the sensitivity C obtained from the calibration done at the temperature T_0 and the voltage V_0 derived from eq. (1) and expressed as a function of T and V :

$$E = \frac{V_0(T, V)}{C} = \frac{V(T) - a - b(T - T_0) - c(T - T_0)^2}{C} \quad (2)$$

The coefficients a , b , and c in Eq. (1) and (2) were derived from the best fit of a second order polynomial to the measured curves (Figure 21). They are listed in Table 8 for each of the eight pyranometers, together with the root-mean square error ($RMSE_{corr}$) remaining after applying Eq. (1) and the $RMSE$ that was present before applying it. This last error was estimated based on the deviations of the voltage outputs measured in the range $\pm 30^\circ\text{C}$ from the value measured at the calibration temperature. The $RMSE_{corr}$ reads as:

$$RMSE_{corr} = \sqrt{\sum \sigma_V^2 / n - 1 + RMSE_{poly}^2} \quad (3)$$

where n is the number of averaged voltage outputs (7 in this case, corresponding to the 7 selected temperatures in the range $\pm 30^\circ\text{C}$) and $RMSE_{poly}$ is the root-mean-square-error of the polynomial fit to the averaged voltage outputs.

Table 8: Coefficients a , b and c of Eq. (1) and (2) derived from the best fit of a second order polynomial for the eight pyranometers, as well as the root-mean square error ($RMSE_{corr}$) remaining after applying Eq. (1) and the $RMSE$ that was present before applying it.

Pyranometer	Thermal correction coefficients			$RMSE_{corr}$ (V)	RMSE before correction (V)
	a (V)	b (V/ $^\circ\text{C}$)	c (V/ $^\circ\text{C}^2$)		
CNR1 071368 upper	1.2069e-07	-4.2063e-07	-1.0445e-08	2.1772e-06	1.7051e-06
CNR1 071368 lower	1.2910e-07	-5.2193e-07	-1.1302e-08	1.3822e-06	1.9106e-06
CNR1 080025 upper	1.2253e-07	4.3892e-07	-1.0341e-08	3.7121e-06	1.1407e-05
CNR1 080025 lower	1.4740e-07	-1.9567e-09	-1.2331e-08	2.7561e-06	7.0798e-06
CNR1 080069 upper	2.7713e-07	-2.1033e-06	-2.1405e-08	3.1896e-06	1.6210e-05
CNR1 080069 lower	1.9544e-07	-2.4574e-06	-1.6687e-08	3.4523e-06	2.3197e-05
CNR4 090113 upper	2.5458e-07	-9.8014e-07	-2.6756e-08	2.8463e-06	4.5006e-06
CNR4 090113 lower	2.5973e-07	-9.0624e-07	-2.6732e-08	2.4140e-06	4.9026e-06

These estimated $RMSE_{corr}$ give the 68% probability that the true voltages are in the given uncertainty interval around the corrected outputs. Since the sensitivity C of the pyranometers is in the order of $\sim 10 \mu V/W/m^2$, $RMSE_{corr}$ the remaining error in broadband irradiance associated to the drift of sensitivity with temperature after applying Eq. 2 is well below $1 W/m^2$ for all instruments. The error present without the thermal correction (the last column in Table 8) is, in some cases, one order of magnitude bigger than $RMSE_{corr}$ (resulting in an error in broadband irradiance up to $5 W/m^2$ for some temperatures) while in other cases it is comparable to $RMSE_{corr}$. These results highlight the need of thermal characterization of the pyranometers, to identify which of them is most sensitive to the temperature and needs a thermal correction.

Angular characterization

To measure the angular response of the pyranometers, the dual-axis rotation stage shown in Figure 18 was installed on the optical table and its horizontal rotation axis was aligned with a pre-burned 250 W lamp. The sensing surface of the pyranometer under characterization was centered in the crossing of the two rotation axes, to enable the measurement of the zenith and azimuth response of the pyranometers with a sequence of horizontal and vertical rotations. The sensor's response at different zenith angles was measured every 6 degrees between 0° and 90° zenith angles. These measurements were repeated 6 times for two azimuthal directions: the south-north direction (aligned with the main axis of the instrument) and the east-west direction (perpendicular to the main axis of the instrument). Measurements were taken at 2 seconds interval and 1-minute averages were used in the calculations. Figure 22 illustrates the percentage errors in the cosine response of the pyranometer pairs (upper and lower) of the considered CNR1 and CNR4 net-radiometers as a function of the solar zenith angle: the vertical bars indicate the standard deviations over 4-6 measurements (few measurements were discharged because of issues with the thermal drift of the measuring pyranometer). All the pyranometers underestimate the irradiance (the percentage error is negative) and the errors increase with increasing solar zenith angle. However, the slope of the error increase with solar zenith angle differs quite a lot among the sensors: for instance, at 78° zenith angle the relative error ranges from $-6.1 \pm 1.2\%$ (Upper CNR1 080069) to $-11.6 \pm 3.3\%$ (Table 9). Hence, these results highlight the need of individual angular characterization of all the pyranometers of the PROMICE and GC-Net network, to improve the accuracy and the consistency of the broadband irradiance and albedo measurements.

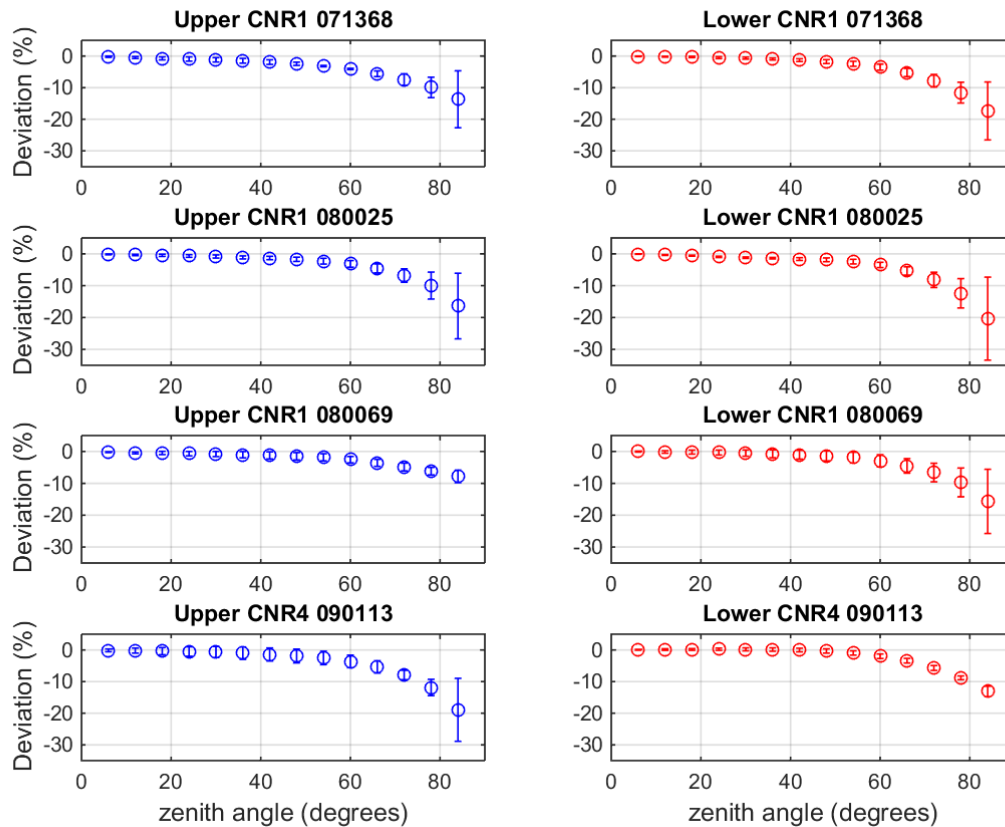


Figure 22: Measured deviations from the perfect cosine response (circles) and their standard deviations (vertical bars) for the pyranometers of the considered CNR1 and CNR4 net-radiometers.

Table 9: Measured deviations from the perfect cosine response (in percentage) and their standard deviation for the pyranometers of the considered CNR1 and CNR4 net-radiometers.

Zenith angle	CNR1 071368 upper	CNR1 071368 lower	CNR1 080025 upper	CNR1 080025 lower	CNR1 080069 upper	CNR1 080069 lower	CNR4 090113 upper	CNR4 090113 lower
6	-0.2 ± 0.2	-0.1 ± 0.1	-0.2 ± 0.1	-0.1 ± 0.1	-0.2 ± 0.2	-0.0 ± 0.1	-0.1 ± 0.4	0.1 ± 0.1
12	-0.5 ± 0.3	-0.2 ± 0.1	-0.4 ± 0.2	-0.4 ± 0.2	-0.4 ± 0.3	-0.1 ± 0.4	-0.2 ± 0.8	0.1 ± 0.2
18	-0.7 ± 0.5	-0.3 ± 0.2	-0.5 ± 0.4	-0.6 ± 0.2	-0.5 ± 0.5	-0.2 ± 0.6	-0.4 ± 1.1	0.2 ± 0.3
24	-0.9 ± 0.7	-0.5 ± 0.3	-0.7 ± 0.4	-0.9 ± 0.2	-0.6 ± 0.7	-0.3 ± 0.8	-0.5 ± 1.5	0.2 ± 0.4
30	-1.2 ± 0.7	-0.7 ± 0.3	-0.8 ± 0.5	-1.2 ± 0.2	-0.8 ± 0.8	-0.5 ± 1.0	-0.6 ± 1.7	0.2 ± 0.5
36	-1.5 ± 0.7	-0.9 ± 0.3	-1.1 ± 0.5	-1.4 ± 0.2	-1.0 ± 1.0	-0.7 ± 1.2	-1.0 ± 2.0	0.2 ± 0.5
42	-1.9 ± 0.7	-1.3 ± 0.4	-1.3 ± 0.5	-1.6 ± 0.4	-1.2 ± 1.2	-1.0 ± 1.4	-1.4 ± 2.0	0.0 ± 0.6
48	-2.4 ± 0.5	-1.7 ± 0.6	-1.7 ± 0.7	-1.9 ± 0.6	-1.5 ± 1.1	-1.4 ± 1.5	-1.9 ± 2.2	-0.3 ± 0.7
54	-3.2 ± 0.2	-2.4 ± 0.8	-2.3 ± 0.9	-2.4 ± 0.7	-1.8 ± 1.1	-1.9 ± 1.7	-2.5 ± 2.1	-0.9 ± 0.7
60	-4.1 ± 0.2	-3.5 ± 0.9	-3.2 ± 1.0	-3.5 ± 0.8	-2.6 ± 1.0	-2.9 ± 1.9	-3.6 ± 2.0	-2.0 ± 0.7

66	-5.6 ± 0.9	-5.2 ± 1.3	-4.6 ± 1.4	-5.4 ± 1.3	-3.6 ± 1.1	-4.5 ± 2.3	-5.3 ± 1.9	-3.4 ± 0.7
72	-7.4 ± 1.8	-7.8 ± 2.0	-6.8 ± 2.1	-8.1 ± 2.4	-4.9 ± 1.2	-6.6 ± 2.9	-7.9 ± 1.5	-5.7 ± 0.8
78	-9.9 ± 3.2	-11.6 ± 3.3	-9.9 ± 4.2	-12.4 ± 4.6	-6.1 ± 1.2	-9.7 ± 4.5	-11.8 ± 2.6	-8.8 ± 0.6
84	-13.7 ± 9.0	-17.3 ± 9.2	-16.4 ± 10	-20.3 ± 13	-7.8 ± 2.0	-15.6 ± 10	-18.9 ± 10	-13.0 ± 1.6

2.3.4. Accessibility of the obtained upgraded data sets and repositories used

The developed equations for thermal correction of pyranometers can be included in the automatic processing of the raw data of the current PROMICE data management. The measured cosine response errors are only the first part of a more complex procedure that needed to be developed to correct the solar radiation measurements for the error caused by the deviation of pyranometers from the perfect cosine response.

We have plans to develop an automatic procedure that can also be implemented in the automatic and near-real time data processing flow (see section 2.3.5).

2.3.5. Future plans for operation of the observing system, including data provision

In collaboration with GEUS, we plan to extend the characterization to the other pyranometers installed in the PROMICE and GC-Net networks of automatic stations in Greenland (about 40 stations).

The deviation of the response of pyranometers from the perfect cosine response is a major error source for the broadband irradiance and albedo observations at the high latitudes, and the laboratory characterization of the instruments is only a first step of the procedure that should be developed to correct for this error.

We plan to carry out the subsequent steps in collaboration with GEUS, to generate a correction algorithm that can be implemented in the automatized data management.

The broadband irradiance and albedo data collected by the PROMICE and GC-Net networks of automatic weather and ice stations are key data for Greenland surface energy and mass budget estimations as well as for glaciological, hydrological, and weather and climate modelling and process understanding.

The data also represent the important ground-truth to validate cryospheric remote sensing products and model outputs. Therefore, the improvement of the data accuracy is of very high relevance, especially now that the two networks (PROMICE and GC-Net) are under the same management and can develop in a coordinated effort.

2.4. UPM

Contributors: Francisco Navarro, Evgeny Vasilenko, Eva de Andrés

2.4.1. Results of the final implementation of the observing system

The instrument developed during the project duration is a new version, initially named VIRL8, of the already available ground-penetrating radar (GPR) VIRL7 (Vasilenko et al., 2011). The planned main differences were in terms of its internal parameters, in the construction of the control and recording unit (CRU) and in the structure and switch type of the transmitter.

A detailed description of the system was included in Section 3.4 of Deliverable D3.1. In summary, the radar system consists of two main parts: transmitter (TX) and receiver (RX), both connected by an optical synchronization link. The RX includes the control and recording unit (CRU) and a receiver amplifier (RA). Additionally, the system includes two antennas, external batteries, and optionally a GPS receiver and an odometer (Figure 23). Unfortunately, due to a heart attack, followed by bypass surgery and retirement of the electronic engineer in charge of the project, not all of the initially planned improvements could be implemented. In particular, an improved transmitter was developed and field-tested, but the CRU remains the same as in VIRL7. For this reason, we have renamed this new version VIRL7a instead of VIRL8.

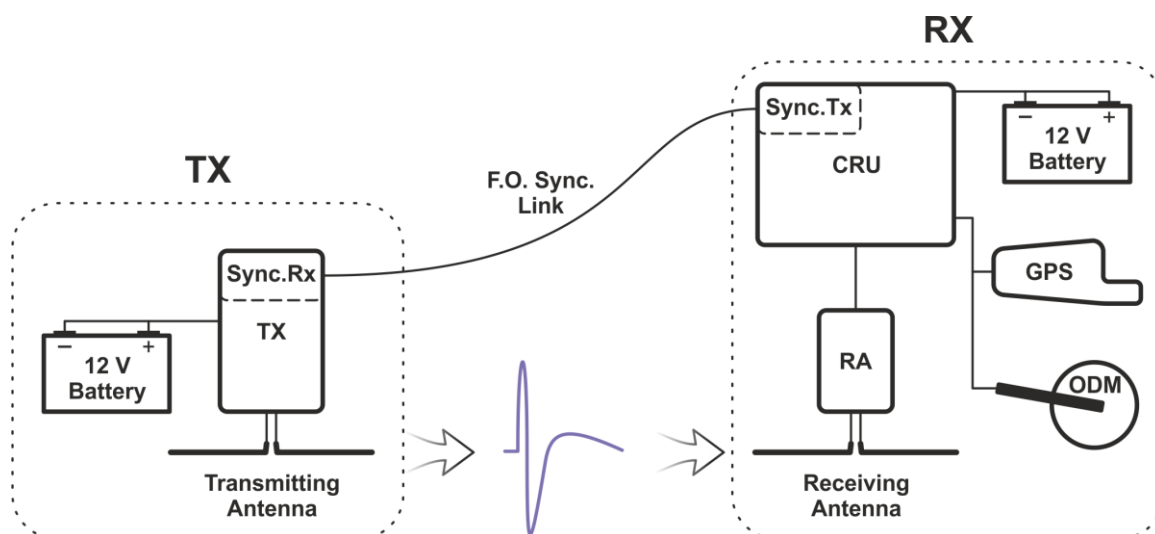


Figure 23: Block diagram of VIRL7a.

The equipment was successfully field-tested taking advantage of an already-scheduled field campaign in Livingston Island, Antarctica, with the logistic support of the Spanish Antarctic Station Juan Carlos I (JCI). The test was done on 14 January 2019, using the Bell 412 helicopter on board of the Colombian Navy ship “ARC 20 de Julio”, during its visit to JCI Station (Figure 24). The field testing was actually a complete data set collection along ca. 200 km of radar lines, as detailed in Section 2.4 of Deliverable D3.6. Further details on the data and its processing are given in Section 2.4.3 below.



Figure 24: VIRL 20 MHz radar system mounted on a frame about to be lifted by a Bell 412 helicopter.

There was a plan to develop a full campaign, using this equipment, in the vicinity of Qaanaaq, north-western Greenland, in early spring 2020. The target was the radio-echo sounding of the calving front of Bowdoin Glacier, as well as the highly-crevassed fronts of other neighbouring glaciers such as Verhoeff, Hubbard, Tracy and Heilprin.

Unfortunately, this planned field campaign had to be cancelled due to the COVID-19 pandemic. Moreover, it could not be re-scheduled for spring 2021, for two reasons: 1) the high uncertainty about the status of the pandemic for spring 2021, and 2) the fact that most of the funding for this campaign was not from INTAROS but from a project funded by the Spanish State Plan of R&D, ending in December 2020.

Consequently, no ice-thickness data collection with this instrument has been possible in Arctic glaciers (Greenland, in particular) during the duration of INTAROS project. The only data collection has therefore been that done in Antarctica mentioned above (originally designed as a field test) and detailed in Section 2.4.3.

2.4.2. Lessons learned and technology challenges identified during the project

The reason behind the development of this radar system was to allow its operation close to the calving fronts of tidewater glaciers or floating ice tongues, where the strong scattering and large signal energy losses produced by the highly-crevassed areas next to the calving fronts often prevent the identification of the bed reflection, and hence determining the ice thickness.

The new radar system developed by UPM under INTAROS contributed to overcome this difficulty by providing a high-energy radar system (much energy concentrated into a very narrow wavelet) with large signal stacking capabilities, whose operation, including the setting of the recording parameters, can be remotely controlled from the helicopter cabin. Having data on ice thickness near the calving fronts is crucial to assess the ice flux into the ocean and the processes governing this flux.

Our field tests have revealed that the main challenge, from the logistic point of view, is avoiding (for data collection) the periods past the onset of glacier surface melting, as this results in much water at the glacier surface and within the frontal crevasses, impeding the propagation of the radar signal deeper into the glacier and therefore preventing the identification of the bed reflection, and hence the determination of ice-thickness near the calving fronts. Another challenge is the presence of nunataks causing strong lateral reflections of the transmitted radar signal, which mask the bed reflection. As this is physically unavoidable, developing software tools allowing to cancel the effects from these lateral reflections and enhancing the bed reflection is a priority task.

2.4.3. Description of processing and analysis of the obtained data

The radio-echo sounding done in Livingston Island, Antarctica, on 14 January 2019, consisted of 200 km of helicopter-borne radar profiles as shown in Figure 25 (left panel). The variable measured was ice-thickness, and the aim was to collect data above the highly-crevassed calving fronts present in most of Livingston Island ice cap periphery, where radar profiling from the glacier surface is not possible. A measurement was taken every 0.2-0.3 s, which, considering a helicopter velocity of ca. 75 km/h, means an ice-thickness measurement every 5 m approximately. The data processing was done using ReflexW software (<https://www.sandmeier-geo.de/reflexw.html>). The main processing steps consisted of bandpass filtering, normal move-out correction, amplitude correction and migration (e.g., Navarro and Eisen, 2010). Deconvolution was not used because our pulse duration is small (ca. 25 ns) and thus there is no need to shorten it. For time-to-thickness conversion we used a constant radio-wave velocity of 0.168 m/ns.

It has not been possible to get a clear bed reflection along the whole set of profiles collected. Several reasons have contributed to this. On one hand, the radio-echo sounding had to be done (for logistic reasons) at a more advanced time in the campaign than initially planned (mid-January, instead of the planned mid-December), with the consequence that glacier surface melting had already been initiated. Much of this surface meltwater goes into the frontal crevasses, resulting in strong backscattering of the transmitted radar signal, preventing its penetration deeper into the glacier. On the other hand, the presence of various nunataks emerging through the ice cap cause multiple lateral reflections of the transmitted radar signal, which mask and make very difficult, sometimes impossible, to clearly identify the glacier bed reflection (see an example in Figure 25 right panel).

We still hope that further efforts and data-processing developments will allow the retrieval of glacier bed signal from additional sections of the radar profiles.

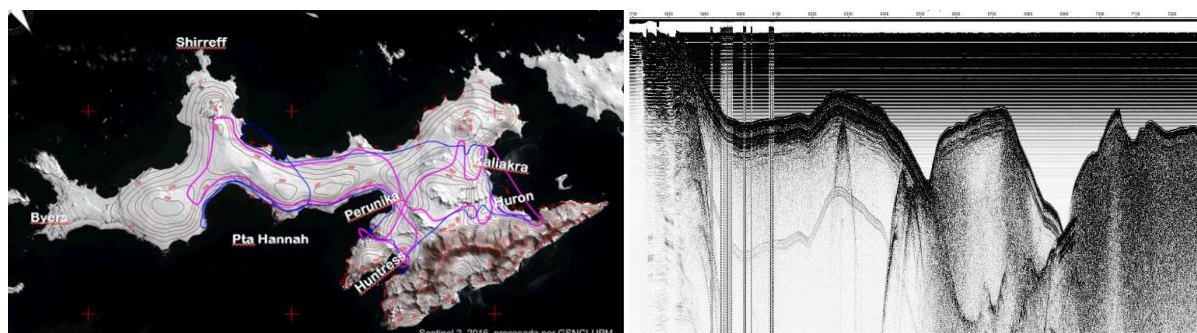


Figure 25: Left: GPR lines performed on Livingston Island (blue lines), Antarctica, on 14 January 2019, using VIRL 20 MHz radar system from helicopter. The magenta lines represent the GPR lines originally planned. Right: a sample radargram collected during the helicopter-borne GPR profiling.

2.4.4. Accessibility of the obtained data sets and repositories used

The collected data, upon use in scientific publications, will be stored and made publicly available, together with the associated metadata, through the Glacier Thickness Database (https://www.gtn-g.ch/data_catalogue_glathida/; GlaThiDa Consortium, 2019; Welty et al., 2020), maintained by the World Glacier Monitoring Service (WGMS) for the Global Terrestrial Network for Glaciers (GTN-G).

2.4.5. Future plans for operation of the observing system, including data provision

Future plans include further collection of ice-thickness data, close to the calving front of tidewater glaciers and floating ice tongues, both in the Arctic and in Antarctica, to be used for ice discharge and calving flux estimates.

Target regions are Svalbard, in the Arctic, and the South Shetland Island, in the Antarctic Peninsula Region, mostly due to secured logistic support. The relevant variable is ice-thickness, and the collected data, upon processing and use in scientific publications, will be stored and made publicly available through the GlaThiDa database (https://www.gtn-g.ch/data_catalogue_glathida/), as done with most of our previously collected data.

2.5. CNRS-Takuvik

Contributors: Marcel Babin, Claudie Marec

2.5.1. Results of the final implementation of the observing system

A sensor was developed to measure vertical profiles of the inherent optical properties (IOPs) of sea ice using spatially resolved diffuse reflectance. The probe we developed was successfully deployed in May 2019 in Baffin Bay, Canada and a publication regarding these operations was submitted to the EGU journal *The Cryosphere* last March. Furthermore, the probe was deployed in spring and summer 2020 in high Arctic during the MOSAIC Joint International Expedition onboard the RV *Polarstern* with the aim to measure IOPs seasonal evolution. A publication in collaboration with international partners from Alfred Wegener Institute is on the way.

Two other sea-ice sensors have been developed at Takuvik, namely a radiance camera and a nitrate sensor. The radiance camera will allow to measure radiance angular distributions within sea ice. These measurements will be used to develop better structural-optical relationships that would help developing better light transport models. Takuvik also developed an improved method to measure nitrate using a custom-made liquid waveguide capillary cell spectrophotometer and designed a 12V battery-powered instrument ideal for in situ observations. These two sensors have been characterized and tested in the laboratory, unfortunately the field tests were scheduled in May 2020 and postponed until 2022 due to COVID restrictions to access northern locations.

2.5.2. Lessons learned and technology challenges identified during the project

The access to the field location is the main challenge for in situ measurements and testing the developed sensors, especially during COVID restrictions.

Regarding the technological challenges, for the nitrate sensor, the main limitation is the measurements of nitrates within the brine channels, rather than the nitrate within the sea-ice as a whole. An approach that is under evaluation is the use of the sackhole approach, where a hole is produced using a sea-ice corer, to a specific depth and brine leaks in the hole and pumped for measurements.

The integration of all of the sensors to the sea-ice endoscope and the development of the sea-ice endoscope itself also prove to be technologically challenging, to match all the requirements for in situ observations and to physically integrate the different new sensors.

2.5.3. Description of processing and analysis of the obtained data

In addition to the classical optical properties on the water column measured under the sea ice (radiance, irradiance, absorption, backscattering, chlorophyll-a, nutrients), Takuvik has developed three sensors to measure, within the sea-ice, the spatial variability of the inherent optical properties (IOPs - absorption and backscattering), the radiative field and the nitrate concentration.

For IOP measurements, the diffuse reflectance method used to measure the IOPs of human tissues was adapted to sea-ice. The instrument emits light into the ice through an optical fibre. Backscattered light is measured at multiple distances away from the source using several receiving fibres. Comparison to a Monte Carlo simulated lookup table allows to retrieve the absorption coefficient, the reduced scattering coefficient and a phase function similarity parameter γ .

To assess the radiative field, a custom radiance camera was designed and assembled to improve the radiometric quality of the measurements, reduce the size (and therefore the footprint) and allow better control over the acquisition parameters. The prototype was calibrated and characterized in laboratory and field validated using freshwater ice.

The nitrate concentration was estimated using an UV spectroscopic approach, with a custom-made liquid waveguide capillary cell (LWCC) spectrophotometer. A graphical user interface has been designed to display instantaneously the nitrate concentration as well the temperature and salinity of the analyzed sample. Our prototype has been tested in the laboratory on samples from the Labrador Sea (2016), Churchill River (2014) and Baffin Bay (2016). Results have shown better accuracy and precision relative to currently used instruments based on UV absorption spectroscopy suggesting that LWCCs spectrophotometer is a promising technique for real-time nitrate monitoring in seawater and sea ice.

2.5.4. Accessibility of the obtained data sets and repositories used

The methods will be published in international journals in 2021. Once all sensors are integrated to the sea-ice endoscope, a data paper with all data collected in Qikiqtarjuaq will be published and data will be publicly available. Meanwhile, the data are archived on the Takuvik repository at Université Laval, known as the Valeria repository system for research applications. The data are stored with redundancy to ensure no losses of the findings.

2.5.5. Future plans for operation of the observing system, including data provision

A research station with two laboratories, storage space and accommodations for the researchers will be constructed over the next three years in Qikiqtarjuaq. This facility will significantly augment the access to the field site and the laboratory analyses required to validate the field measurements.

Takuvik intends to continue measuring sea-ice properties in Qikiqtarjuaq and other coastal ecosystems in Baffin Bay. The sensors developed at Takuvik will be integrated to a sea-ice endoscope in development at Université Laval. This endoscope will optimize the acquisition of data in situ over a wide range of sea-ice geometries.

3. Performance and fitness-to-purpose of the platforms, sensors and systems implemented during INTAROS for a future sustained Arctic observing system

3.1. GEUS

Snow water equivalent sensors

Annual snow mass or snow water equivalent (SWE) from snowfall in Greenland is a major mass budget term. The new sensor measures how much mass that accumulates as snow during the winter season on the Greenland ice sheet. The system shows promise and the SWE measurements fully complement the other instruments to monitor changes in the daily surface mass balance from the PROMICE automatic weather stations. We do plan adjustments to the system so that it measures for a longer period of time before sensor and datalogger goes into power-save mode.

Presently, the SWE measurements will still be kept as a separate system alongside the PROMICE station in order not to jeopardize the core station operation. Eventually, the SWE sensor will be integrated in the standard station setup and established at all the stations where these parameters are relevant. In terms of data assimilation, logistics and instrument maintenance, the SWE sensor will be maintained, and data will be downloaded during regular PROMICE visits. On a yearly basis, we integrate all future adjustments and measurements of the dataset and update the data product on the PROMICE data portal.

High accuracy GNSS positioning

The GNSS device is fit for application both as a standalone unit for applications such as monitoring of ice velocities and as a component of larger systems such as the PROMICE automatic weather stations (AWS). The very low power consumption makes allows implementation anywhere year-round operation in the Arctic is required. Considering the much lower price, weight, size and power consumption, when compared to permanent GNSS installation such as those part of GNet which would be impossible to deploy on ice, the data quality is very satisfactory.

The logistics requirements both for installation and maintenance are no different than a PROMICE AWS for a standalone GNSS unit and can easily be installed at the same time of the AWS. Costs-wise, after the initial purchase cost the only operating costs are for data transmission via satellite and, if desired and available on the market, the subscription to L-band PPP augmentation services.

There are three promising avenues for further development. The first is adding a terrestrial data link capability so that differential processing over baselines of in the order of some kilometers becomes possible. The second is a drop-in compatible carrier board to replace the current dual/triple frequency OEM GNSS receiver with lower cost dual frequency modules that have come to the market during the recent years, for use in more cost-sensitive applications where a slightly lower positional accuracy may be acceptable. The third is to develop a more tailored data processing workflow that takes full advantage of the very constrained dynamics of a receiver moving down-glacier, in order to obtain the highest possible positional accuracy from the limited amount of data that can be easily transmitted via Iridium.

Azimuth and tilt sensors

While the technical difficulties encountered during the 2019-2020 test field season of the INTAROS azimuth and tilt sensor on Qasigiannuit Glacier close to Nuuk, Greenland have delayed the operational deployment of the instrument, the performance of the sensors in the lab matched expectations.

The actual device has been designed with spare power and digital inputs sufficient for extending the system with low-cost mini-spectrometers which, while having rather low performance, are also cheap and able to operate at sufficiently low power to be deployed year-round at several AWS.

Rain gauges

Precipitation gauge undercatch errors and correction efforts are widely documented, e.g. Førland et al., 1996; Goodison et al., 1998; Sevruk et al., 2009. In Greenland rainfall studies, various undercatch corrections have been applied to coastal precipitation gauges operated by the Danish Meteorological Institute by e.g., (Mernild et al., 2015; Yang et al., 1999; Koyama and Stroeve, 2019; Niwano et al., 2021); Huai et al (2021). In addition to precipitation undercatch that results from distortion of the windfield around the rain gauge by the measurement platform and the gauge itself (Sevruk et al., 1991), error sources include unknown precipitation phases. Here, we consider only liquid precipitation (rainfall) by excluding cases with hourly air temperatures under +1 °C. Nonetheless, the gauges deployed on the PROMICE stations may accumulate snow and thus can bias rainfall date and amount from delayed snow melt. We thus consider field data only after mid-June when all such snow would have ablated. We found no evidence that the TR-525I tipping mechanism moves under high wind speed conditions, and thus produced a spurious precipitation signal.

Cohesion and evaporation losses

Precipitation undercatch also results from 1.) water droplet adhesion around the inlet to the tipping mechanism, i.e. 'wetting loss' and includes evaporation of the droplets before the mass flux can be registered. Rain water that is insufficient to drain through to reach the tipping mechanism counts as trace precipitation. The evaporation and wetting losses increase in importance when total precipitation is low (Yang et al 1999), i.e. at the arid locations KAN_L and KAN_B.

TR-525I instrument level concerns

The PROMICE weather station and thus the TR-525I instrument is not always level. When not level, the tipping function can be prevented, leading to an underestimate of actual rainfall. Based on this consideration, we found no obvious tendency for more spurious wet bias in the comparisons of the field data with the atmospheric model data. We nevertheless limit our comparison to those data having a tilt smaller than 5.6° , which is the tilt recorded during the 14-15 September 2017 extreme rain event at QAS_M. For the relatively small sample of QAS_U data (because the record started in 2018 and temperatures are lower), a tilt of $\sim 18^\circ$ prevents the use of most of those data.

INTAROS has catalysed a new era of rainfall observations from Greenland ice sheet locations. The timing is good considering how both observations and modelling efforts find rainfall increasing in Greenland (Niwano et al., 2021) the Arctic (AMAP, 2021).

3.2. AU

The purpose of the deployed instruments was to provide reliable data collection on sub-hour resolution to document decadal scale changes in hydrographic conditions in a NE Greenland fjord. Since instruments are deployed for a year at the time, high reliability of the system is necessary to obtain a continuous data series. The performance of the instruments used was very good. So far, the two instruments have worked for two years, without problems.

We plan to retrieve the instruments in August, which hopefully results in three consecutive years of observations. Funding for maintenance, calibration and logistics is in place and the instruments will contribute to the sustained monitoring in Young Sound as part of the Greenland Ecosystem Monitoring Programme.

3.3. FMI

The developed procedures to characterize the thermal and angular response of pyranometers and, thus, increase the accuracy of the solar irradiance and albedo measurements has been applied to some of the CNR1 and CNR4 net-radiometers of the PROMICE network over the Greenland ablation area managed by GEUS. The results showed that, to increase inter-comparability and accuracy of the measurements, it would be beneficial to extend the thermal and angular characterization also to the other pyranometers of the PROMICE and GC-Net networks, the latter covering the Greenland accumulation area and being recently passed under GEUS management. These characterizations will increase the quality and, thus, the value of the data, and will enhance the cost efficiency of the networks without any additional load to the logistics. The correction algorithms derived from the instrument characterization need further development steps to be applied in the near-real time generation of the irradiances and albedo products. For these advancements in instrument characterization and data processing, the continuation of the collaboration between FMI and GEUS is desirable.

3.4. UPM

The radar system development carried out by UPM under INTAROS constitutes a useful tool for determining the ice thickness in highly crevassed areas near the glacier calving fronts, where ground-based surveys are not feasible. In this way, it provides the capability to improve the knowledge of ice-thickness at the usual locations of the flux gates where solid ice discharge to the ocean is calculated, thus helping to estimate the contribution of ice mass losses to sea-level rise. Consequently, this radar system is a valuable tool to improve the ice discharge estimates in a future sustained Arctic observing system.

Our radar system is especially designed for being used on a wood frame carried under a helicopter, and the typical measurement campaigns should focus on the terminal areas of tidewater glaciers or floating tongues (i.e. often remote areas). Therefore, the main logistic cost of operating the system is the helicopter rental, in addition to the campaign costs (trips, subsistence) of the personnel in charge of operating the equipment (two people are sufficient). Engineer time for maintenance of the equipment is also required, but our experience is that this cost is not overly high, because the system is rather robust.

The quality of the data collected is strongly dependent on the glacier conditions, in particular regarding glacier melt. The radar campaigns should be done before the onset of melt. Otherwise, the strong reflectivity of the radar signal by surface meltwater (or water in crevasses) prevents the penetration of the radar signal deeper in the ice, and thus the possibility of detecting a bed return. Even for data collected under favorable conditions, a detailed and time-consuming radar data processing by an experienced user is required, because the intense crevassing near the glacier fronts causes a mesh of radar reflections and diffractions, often overlapped with radar returns from the glacier sidewalls (mountains surrounding the outlet glacier), so that detecting the bed return is not an easy task.

Summarizing, radar campaigns are rather expensive, require specialized personnel both for the campaign and for the subsequent data processing, as well as for the occasional equipment maintenance. Consequently, they normally rely on research funding data through specific projects. In spite of its cost, they can provide extremely useful data for the estimates of solid ice discharge and hence for the study of the contribution of glacier mass losses to sea-level rise.

3.5. CNRS-Takuvik

The sea-ice sensors developed at CNRS-Takuvik, once integrated to the sea-ice endoscope, will provide a suite of in situ bio-optical measurements within sea ice. This efficient platform will be easy to transport and to deploy in various coastal environments where sea ice may take various forms (landfast ice, multiyear ice, ridges, etc.). The data that will be gathered from this platform will greatly improve the modelling of the sea-ice itself as well as the light field of the underneath water column.

Moreover, the research station that will be constructed in Qikiqtarjuaq, as announced by the Canadian Foundation for Innovation in February 2021, will offer an easy, affordable and safe access to the nearby landfast ice and underneath coastal marine ecosystem representative of the Baffin Bay Arctic waters.

4. Summary

The work done in INTAROS WP2 to obtain an overview of Arctic observation systems and parameters, includes reports on present capabilities, gaps and exploitation which points to a significant potential for increased synergy within and between different spheres.

The present report only details work done within INTAROS in one of the reference sites, Coastal Greenland, but serves as a useful example of what may be accomplished over time on a larger scale. Cutting across established fields of research, bridging widely different applications, acknowledging the transnational character of the Arctic climate change challenge, INTAROS proves how we can make better use of our monitoring resources and make a focused effort to address the most critical observational gaps.

The majority of the work reported here consist of improvement of monitoring system parameter coverage by adding existing sensors already available. Some of the work details actual technical improvement of sensors, like the VIRL ice-penetrating radar system of UPM, the assembly of a GNSS precise-positioning device suitable for automated measurements in extreme conditions and the collaboration between FMI and GEUS on improving the precision of shortwave radiation measurements on the Greenland ice sheet.

Overall, the Task 3.1 work at the Coastal Greenland reference site deals with the impact of changes in the Arctic water and ice cycle on the physical and biological environment. Starting on the ice sheet by monitoring the amount of snow and rain precipitation, improving albedo measurements to qualify meltwater formation modelling and conducting precise ice-velocity measurements. All these parameters increase confidence in the solid and liquid freshwater transport to the ice margin, where improved ice thickness measurements help characterize the transition of the ice and meltwater to the fjord systems and surrounding ocean. In this domain, the monitoring of the impact of the freshening on the marine ecosystem, the physical characteristics and the ocean CO₂-uptake is improved.

Below, in Table 4.1, an overview of the results in Task 3.1 is provided.

Table 4.1. Final results in Task 3.1.

Partner	GEUS
Action	Snow-water equivalent on the ice sheet
Objective	To reduce uncertainty in meltwater output to the ocean
Instrument development	None, except power supply
Field deployment	Summer 2018 - 5 instruments at four locations on the Greenland ice sheet
Challenges	Insufficient power supply during winter/snow burial
Final results	Data on snow water equivalent (SWE) successfully retrieved from SnowFox instruments and processed from four sites co-located with PROMICE weather stations, power supply issues were identified, and mitigation measures taken. The demonstrated SWE measurement will be rolled out for additional PROMICE weather stations over the coming years and data made openly available through the PROMICE database.

Partner	GEUS
Action	Precise positioning of ice sheet stations
Objective	To calibrate satellite-derived ice velocity maps and numerical weather prediction
Instrument development	Yes, assembling new type of GNSS unit with antenna and communication/control
Field deployment	Summer 2019 (test unit)
Challenges	Complications in the communication between parts of the assembly caused delays in field deployment, limiting test deployment to one site in 2019
Final results	High-precision vertical and horizontal positional data was successfully retrieved from the new GNSS unit, capable of recording e.g. ice ablation by accurately recording changes in elevation. The deployment successfully tested a range of possible issues and a modified version of the device has already been implemented in experimental landslide monitoring. The GNSS unit will be rolled out on further ice sheet and glacier weather stations over the coming years and data made openly accessible to enhance the value of existing AWS data products significantly.

Partner	GEUS
Action	New radiometer tilt and azimuth instrument for improved radiation correction
Objective	To correct the radiation measurements with improved tilt and new azimuth data, because automatic weather stations operating on ice cannot provide a stable level orientation of the radiometers
Instrument development	Yes, assembling new type of tilt/azimuth unit with communication and control
Field deployment	Summer 2019 (test unit)
Challenges	Problems with powering and interfacing to the ADIS16209 resulting in occasional lock-ups during testing, as well as difficulties implementing the planned serial communication using the SDI-12 protocol. First field deployment 2019-2020 resulted in corrupted flashcard and thus no data.
Final results	A rugged, precise and low-power tilt and azimuth sensor was developed and tested in the lab. First field deployment yielded a corrupted flashcard, possibly from sudden power loss during data writing, emphasizing the vulnerability of this data storage method. A second deployment is ongoing.

Partner	GEUS
Action	Rain gauges on ice sheet stations
Objective	To observe rain events and their magnitude on the ice sheet
Instrument development	None
Field deployment	Rain gauges deployed during and prior to the INTAROS effort from 2016 and onwards. The rain gauges are planned to eventually be deployed on all relevant AWS on or near the Greenland ice sheet
Challenges	The undercatch correction is substantial and needs field validation
Final results	Corrected rain datasets from the ice sheet have been successfully retrieved and compared to results from regional climate models and reanalysis products. Rain gauges are now being implemented as a new observation on PROMICE, GC-Net and GEM monitoring weather stations on ice in Greenland

Partner	AU
Action	Snow cover on sea ice
Objective	To study the impact of freshening on the marine ecosystem
Instrument development	None
Field deployment	Aug 2018 – Aug 2019
Challenges	A new camera system to monitor conditions above the instrument in the inner fjord, deployed in August 2018 was found broken in August 2019. It appears to have been damaged by musk oxen. The system was serviced and replaced and is hopefully taking daily images for the 2019-2020 season
Final results	Two years of CTD data so far successfully retrieved from the marine instruments deployed in Aug 2018 and again in 2019, with a third year expected by Aug 2021. It is planned to continue this monitoring as a part of the GEM monitoring programme

Partner	AU
Action	Surface pCO ₂ and ocean acidification
Objective	To study the impact of freshening on CO ₂ -uptake of the ocean
Instrument development	None
Field deployment	Two coastal cruises in West Greenland 2016 and East Greenland 2018
Challenges	None
Final results	So far 746 observations of the pCO ₂ in the upper 50 m distributed among 120 stations

Partner	FMI
Action	Instrument characterization of in-situ ice sheet albedo measurements
Objective	To obtain improved validation of satellite albedo products
Instrument development	Yes, entirely new laboratory facility constructed
Field deployment	N/A
Challenges	The cooling system of the temperature controlled chamber broke and the consequent need of total replacement of many components caused a one-year delay in the characterization work

Final results	Laboratory instrumentation and procedures to characterize the thermal and angular response of pyranometers, to increase the accuracy of the solar irradiance and albedo measurements has successfully been applied to CNR1 and CNR4 net-radiometers of the PROMICE network. The method is expected to be applied to similar radiometers of the PROMICE, GC-Net and GEM monitoring networks in the future
----------------------	--

Partner	UPM
Action	Improvement of ice-penetrating radar system
Objective	To generate ice thickness data over ice-sheet outlet glaciers
Instrument development	Yes
Field deployment	January 2019, testing the system (Livingston Island, Antarctica)
Challenges	Initially planned fieldwork in Greenland in spring 2019. However, due to logistic reasons, this campaign could not be accomplished. It has been necessary to re-use some modules from the existing radar in the development of the new system VIRL8
Final results	Test flights delivered 200 km of good radar profiles over ice, proving the concept of the new helicopter-borne radar system in the field. The processed radar profiles have successfully yielded bedrock returns in usually difficult glaciological settings near glacier fronts, although partly disrupted by occurrence of meltwater and reflections off nearby nunataks

Partner	CNRS-Takuvik
Action	Improvement of under-ice monitoring
Objective	To observe spring bloom and bio-optical/-geochemical properties
Instrument development	None
Field deployment	Pro-ice BGC Argo floats deployed: five in Spring 2016 (with four in Baffin Bay), seven in Summer 2017, two in Summer 2018, two in Summer 2019.
Challenges	Although the Pro-ice floats are adapted to ice-infested waters, the experiment remains a real challenge. The real reason for the loss of some floats, at the beginning of the experiment remains unexplained, but we could diagnostic a mismanagement of the grounding in the firmware that leads to three losses at least (this problem has been fixed).
Final results	More than 1900 profiles have been acquired so far with unprecedented sets of data with series measured under ice during wintertime. Takuvik intends to continue measuring sea-ice properties in Qikiqtarjuaq and other coastal ecosystems in Baffin Bay. The sensors developed at Takuvik will be integrated to a sea-ice endoscope in development at Université Laval. This endoscope will optimize the acquisition of data in situ over a wide range of sea-ice geometries.

The majority of the technical and system design developments have been implemented and instruments deployed over the 2018 and 2019 field seasons, with most deployments continued through 2020 and 2021. Results so far underline the challenges of operating in a severe and remote environment, with some instruments lost or damaged during field deployment, but also hard-earned success in retrieving unprecedented datasets of key physical, biological and biochemical parameters with innovative instrumentation.

The main challenge of Task 3.1 has been to retrieve or maintain instrumentation in and around Greenland during the COVID-19 pandemic situation in 2020, extending now also into 2021. While some partners managed to gain access to field instrumentation, others were not. Obviously, this limits the ability to conclude finally on the results, although these are mainly postponed until instrument retrieval and data processing would become possible. However, given that the field seasons of 2020 and 2021 were and are cancelled for many partners in Task 3.1, full closure on the originally planned work will only be obtained after the formal ending of the INTAROS project.

Several of the system improvements and datasets reported here provide the basis for activities in WP6: Applications of IAOS towards stakeholders, which is focused on delivering demonstration products from the IAOS, more specifically Task 6.4 Natural hazards in the Arctic and Task 6.5 Arctic greenhouse gases.

5. Literature

AMAP 2021: Arctic Climate Change Update 2021: Key Trends and Impacts. Summary for Policy-makers, Arctic Monitoring and Assessment Programme (AMAP), Oslo, Norway, 16 pp., 2021.

Førland, E. J., Norske Meteorologiske Institutt., and Nordic Working Group on Precipitation (NWGP): Manual for operational correction of Nordic precipitation data, Norwegian Meteorological Institute, Oslo, 1996.

GlaThiDa Consortium (2019). Glacier Thickness Database 3.0.1. World Glacier Monitoring Service, Zurich, Switzerland, doi: 10.5904/wgms-glathida-2019-03.

Goodison, B. E., Louie, P. Y. T., and Yang, D.: Solid Precipitation Measurement Intercomparison, WMO, 1998.

Koyama, T. and Stroeve, J.: Greenland monthly precipitation analysis from the Arctic System Reanalysis (ASR): 2000–2012, <https://doi.org/10.1016/j.polar.2018.09.001>, 2019.

Kratzenberg, M. G., H. G. Beyer, S. Colle and A. Albertazzi (2006). "Uncertainty Calculations in Pyranometer Measurements and Application." 689-698. Proceedings of ISEC2006 ASME International Solar Energy Conference July 8-13, 2006, Denver, CO.77 Downloaded From: <http://proceedings.asmedigitalcollection.asme.org/> on 02/17/2016

Mernild, S. H., Hanna, E., McConnell, J. R., Sigl, M., Beckerman, A. P., Yde, J. C., Cappelen, J., Malmros, J. K., and Steffen, K.: Greenland precipitation trends in a long-term instrumental climate context (1890-2012): evaluation of coastal and ice core records, <https://doi.org/10.1002/joc.3986>, 2015.

Navarro, F. J. and Eisen, O. (2010). Ground Penetrating Radar. In P.Pellikka and W.G. Rees (eds.): Remote sensing of glaciers – techniques for topographic, spatial and thematic mapping, pp. 195-229. CRC Press, Leiden.

Niwano, M., Box, J. E., Wehrlé, W., Vandecrux, B., Colgan, W. T., and Cappelen, J.: Rainfall on the Greenland ice sheet: present-day climatology from a high-resolution non-hydrostatic polar regional climate model, *Geophys. Res. Lett.*, 2021.

Sevruk, B., Hertig, J.-A., and Spiess, R.: The effect of a precipitation gauge orifice rim on the wind field deformation as investigated in a wind tunnel, 25, 1173–1179, 1991.

Sevruk, B., Ondrás, M., and Chvíla, B.: The WMO precipitation measurement intercomparisons, *Atmos. Res.*, 92, 376–380, 2009.

Vasilenko, E. V., Machío, F., Lapazaran J. J., Navarro F. J. and Frolovskiy, K. (2011). A compact lightweight multipurpose ground-penetrating radar for glaciological applications. *Journal of Glaciology*, 57(206), 1113-1118, doi: 10.3189/002214311798843430.

Welty, E., Zemp, M., Navarro, F., Huss, M., Fürst, J.J., Gärtner-Roer, I., Landmann, J., Machguth, H., Naegeli, K., Andreassen, L.M., Farinotti, D., Li, H. and GlaThiDa Contributors (2020). Worldwide version-controlled database of glacier thickness observations. *Earth System Science Data*, 12, 3039–3055, doi:10.5194/essd-12-3039-2020.

Yang, D., Ishida, S., Goodison, B. E., and Gunther, T.: Bias correction of daily precipitation measurements for Greenland, <https://doi.org/10.1029/1998jd200110>, 1999.

----- END of DOCUMENT-----



INTAROS

This report is made under the project
Integrated Arctic Observation System (INTAROS)
funded by the European Commission Horizon 2020 program
Grant Agreement no. 727890.



Project partners:

